NAVAL POSTGRADUATE SCHOOL

MONTEREY, CALIFORNIA

THESIS

COMPUTATIONAL AERODYNAMIC ANALYSIS OF AIRFOILS FOR ENERGY-PRODUCING SAILING SHIPS

by

Susan R. Johnson

June 2020

Thesis Advisor: Anthony J. Gannon
Co-Advisor: Max F. Platzer, Distinguished Emeritus Professor

THIS PAGE INTENTIONALLY LEFT BLANK

REPORT DOCUMENTATION PAGE	*Form Approved OMB No. 0704-0188*

1. AGENCY USE ONLY *(Leave blank)*	**2. REPORT DATE** June 2020	**3. REPORT TYPE AND DATES COVERED** Master's thesis

4. TITLE AND SUBTITLE
COMPUTATIONAL AERODYNAMIC ANALYSIS OF AIRFOILS FOR ENERGY-PRODUCING SAILING SHIPS

5. FUNDING NUMBERS

6. AUTHOR(S) Susan R. Johnson

7. PERFORMING ORGANIZATION NAME(S) AND ADDRESS(ES)
Naval Postgraduate School
Monterey, CA 93943-5000

8. PERFORMING ORGANIZATION REPORT NUMBER

9. SPONSORING / MONITORING AGENCY NAME(S) AND ADDRESS(ES)
N/A

10. SPONSORING / MONITORING AGENCY REPORT NUMBER

11. SUPPLEMENTARY NOTES The views expressed in this thesis are those of the author and do not reflect the official policy or position of the Department of Defense or the U.S. Government.

12a. DISTRIBUTION / AVAILABILITY STATEMENT
Approved for public release. Distribution is unlimited.

12b. DISTRIBUTION CODE
A

13. ABSTRACT (maximum 200 words)

The purpose of this research was to determine an airfoil configuration that produces the maximum amount of thrust on a sailboat that uses a turbine deployed in the water to collect energy. Three airfoil types were analyzed: a single-element airfoil, two-element airfoil, and cloth sail airfoil. A computational fluid dynamics program, ANSYS CFX, was used to perform the analysis. Two key conclusions were observed. The first conclusion is the discrepancy in computational fluid dynamics and the experimental results calculating the drag over a single element NACA 0012 airfoil. An early prediction in flow separation resulted in an overestimation in drag above an angle of attack of eight degrees. The second conclusion is the two-element airfoil was the best configuration to maximize the thrust of a sailboat. After comparing the lift over drag ratio across an angle of attack sweep, the two-element airfoil significantly outperformed the cloth and single-element airfoils.

14. SUBJECT TERMS lift coefficient, drag coefficient, maximum thrust, sail, vessel, airfoil	**15. NUMBER OF PAGES** 95
	16. PRICE CODE

17. SECURITY CLASSIFICATION OF REPORT	**18. SECURITY CLASSIFICATION OF THIS PAGE**	**19. SECURITY CLASSIFICATION OF ABSTRACT**	**20. LIMITATION OF ABSTRACT**
Unclassified	Unclassified	Unclassified	UU

NSN 7540-01-280-5500

Standard Form 298 (Rev. 2-89)
Prescribed by ANSI Std. 239-18

THIS PAGE INTENTIONALLY LEFT BLANK

Approved for public release. Distribution is unlimited.

COMPUTATIONAL AERODYNAMIC ANALYSIS OF AIRFOILS FOR ENERGY-PRODUCING SAILING SHIPS

Susan R. Johnson
Ensign, United States Navy
BS, United States Naval Academy, 2019

Submitted in partial fulfillment of the
requirements for the degree of

**MASTER OF SCIENCE IN ENGINEERING SCIENCE
(AEROSPACE ENGINEERING)**

from the

**NAVAL POSTGRADUATE SCHOOL
June 2020**

Approved by: Anthony J. Gannon
Advisor

Maximilian Platzer
Co-Advisor

Garth V. Hobson
Chair, Department of Mechanical and Aerospace Engineering

THIS PAGE INTENTIONALLY LEFT BLANK

ABSTRACT

The purpose of this research was to determine an airfoil configuration that produces the maximum amount of thrust on a sailboat that uses a turbine deployed in the water to collect energy. Three airfoil types were analyzed: a single-element airfoil, two-element airfoil, and cloth sail airfoil. A computational fluid dynamics program, ANSYS CFX, was used to perform the analysis. Two key conclusions were observed. The first conclusion is the discrepancy in computational fluid dynamics and the experimental results calculating the drag over a single element NACA 0012 airfoil. An early prediction in flow separation resulted in an overestimation in drag above an angle of attack of eight degrees. The second conclusion is the two-element airfoil was the best configuration to maximize the thrust of a sailboat. After comparing the lift over drag ratio across an angle of attack sweep, the two-element airfoil significantly outperformed the cloth and single-element airfoils.

THIS PAGE INTENTIONALLY LEFT BLANK

TABLE OF CONTENTS

LIST OF FIGURES

THIS PAGE INTENTIONALLY LEFT BLANK

LIST OF TABLES

THIS PAGE INTENTIONALLY LEFT BLANK

LIST OF SYMBOLS

δ	identity matrix
$\frac{\partial}{\partial t}$	differential with respect to time
ρ	density
ρ_{spec}	density for specified fluid
τ	stress tensor
μ	molecular viscosity
λ	thermal conductivity

THIS PAGE INTENTIONALLY LEFT BLANK

LIST OF ACRONYMS AND ABBREVIATIONS

BL	boundary layer
CFD	Computational Fluid Dynamics
C_d	coefficient of drag
C_f	coefficient of skin friction
C_l	coefficient of lift
C_p	specific heat capacity at constant volume
C_p	coefficient of pressure
h	specific static enthalpy
h_{tot}	specific total enthalpy
p	pressure
RANS	Reynolds Averaged Navier-Stokes equations
S_E	energy source
S_M	momentum source
SST	shear stress transport
T	static temperature
U	velocity
V_∞	free stream velocity
V_{local}	local velocity

THIS PAGE INTENTIONALLY LEFT BLANK

ACKNOWLEDGMENTS

I would like to sincerely thank several people for their contributions to my thesis effort. Dr. Maximilian Platzer served as my guide to learn about the aerodynamics over sails. He lent an eye rich in experience to make observations that would have gone unnoticed otherwise. Dr. Anthony Gannon provided the guidance to learn ANSYS CFX and to troubleshoot each of my models to obtain fluid flow solutions. Additionally, I would like to thank Dr Garth Hobson for providing the MATLAB code to produce airfoil coordinates and the guidance to create the single element airfoil mesh.

I would also like to thank my parents, Paul and Laura Johnson, for supporting my educational endeavors to attend the Naval Postgraduate School.

THIS PAGE INTENTIONALLY LEFT BLANK

I. INTRODUCTION

A. PROJECT BACKGROUND

This thesis is a part of a larger project to design a hydroelectric sailboat as a method to produce renewable energy. Currently, the U.S. Navy is dependent on fossil fuels to operate many of it ships and all of its airplanes. A renewable energy resource available in the ocean for direct delivery to ships and their aircraft would provide a strategic advantage in the national defense strategy.

In the southern hemisphere in some parts of the ocean, strong westerly winds consistently blow up to 40 or 50 knots [1]. These winds are commonly referred to as the "Roaring Forties," and pose the potential to serve as a reliable renewable energy source given the proper tools. Research has been conducted into the possibility of constructing permanent or mobile platforms in the ocean [1]. A mobile platform is preferred over a stationary platform because it is more versatile and efficient as it can follow the strongest winds [1]. Energy delivery is much simpler with a mobile platform enabling delivery directly to shore [1].

The basic set-up is a sailboat that while under power of sail will be used to force a hydroelectric generator through the water to produce electricity. That electricity may be stored using hydrogen or other methods. The ship with this stored energy would then be sailed to the coastline to deliver energy directly to the grid. The sailboat would then return to the roaring forties to repeat the process. The vision of the project is to produce a fully automated sailboat fleet. This fleet would produce energy with no human intervention required.

B. SAIL DEVELOPMENT

The focus of this thesis was to determine the most effective type of sail to deploy on the hydroelectric sailboats. Three types of airfoils were investigated: a single element symmetric airfoil, a two-element symmetric airfoil, and a traditional cloth sail airfoil. The goal was to determine which airfoil produces the maximum amount of thrust.

1. Sailing Background

Humans have used sailboats for hundreds of years to explore new lands, conduct commerce, and wars. The advent of engines has made sailing as a business and method of war obsolete. In modern times sailing has become a recreation for many and a serious sport for a few. The America's Cup is an international sailing league where teams sail some of the fastest, most advanced sailboats in the world to achieve speeds upward of 30 knots. The America's Cup sailboats provide an example of a highly engineered sailboat design. The missions of the America's Cup and the hydroelectric sailboat which is the focus of the sail design of this paper, vary significantly. The hydroelectric sailboat's mission is to produce maximum thrust and endure turbulent storms in the ocean for months. While the America's Cup sailboat's goal is to go fast for short periods of time in sheltered harbors. Nonetheless, the America's Cup sailboats provide an example and start point for the hydroelectric sailboat sail design.

The America's Cup sailboats traditionally used cloth sails. Recently, with advances the application of CFD and aerodynamic analysis, the wingsail was introduced. A wingsail is typically a two-element, symmetric airfoil similar to the design of an aircraft's airfoil. In the 2010 America's Cup two leading teams, Oracle and Alinghi racing, battled for the championship [2]. Oracle designed a wingsail in addition to its state-of-the-art hull design and went home as the champion [2].

2. Sail Terminology

Figure 1 displays the basic terminology used to reference different parts of a sail's geometry. Traditionally sailboats utilize cloth sails with lines attached to the corner of the sails (the clew). Across the water small changes in wind velocity and direction are observed. To optimize speed a sail is trimmed to accommodate these small changes. Trimming of a sail is accomplished by releasing or tightening the lines attached to the clew. Cloth sails are effective because of their ability to change shape depending on the wind conditions, and their ability to be lowered or raised, reliant on the strength and direction of the wind.

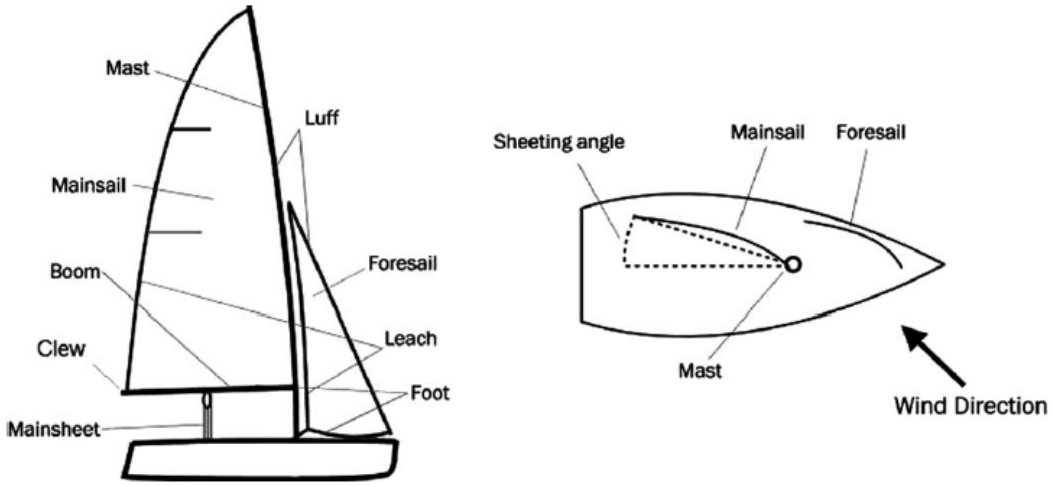

Figure 1. Sailboat diagram. Source: [3]

A typical sailboat has a foresail (jib), on the front of the boat known as the bow, and a mainsail in the center of the boat. The mainsail is the primary thrust generator. The mast serves as the mainsail's primary support system holding the sail vertically from the leading edge of the sail. The boom is located horizontally to the deck of the boat where the clew is tied to support the bottom edge of the sail known as the foot. There are two types of configurations for a sailboat, upwind and downwind. Figure 1 displays the upwind configuration. Figure 2 displays the downwind configuration of a sailboat, using a spinnaker. A spinnaker is a large kite flown out in front of the boat replacing the jib for downwind sailing. Spinnakers allow for faster downwind sailing than a jib.

Figure 2. Blue and gold spinnakers flown on the Naval Academy's Navy 44 Sailboats

A sailboat is capable of sailing at many angles to the wind due to the flexible placement of the jib and mainsail. Figure 3 displays the different angles of sail. Within approximately 30 degrees from the wind direction the sails will stall thus making sailing directly into the wind impossible. It is not safe for a sailboat to sail directly downwind because of the tendency to accidentally jibe. Accidently jibing is a condition caused by a small shift in the wind causing the boom to swings rapidly from one side of the boat to the other. This is very dangerous for any crew onboard and puts the sailboat in a very unstable condition.

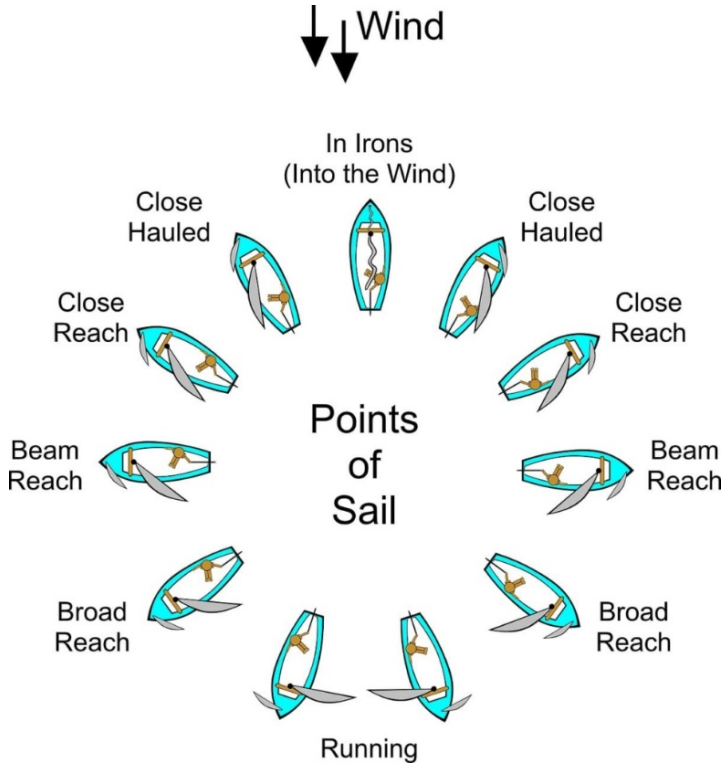

Figure 3. Different angles of sail. Source: [4]

The aerodynamics of sailing are very difficult to research because of the dynamic nature of the sport. The point of sail is always changing; small wind gusts and human adjustment of the sails make predicting and evaluating sail performance very challenging.

C. SAIL AIRFOIL DEVELOPMENT GOAL

The three airfoil types investigated resulted from an observation of the sail's used in the America's Cup and historical sails. The goal was to determine the airfoil configurations best suited to produce maximum thrust for the hydroelectric sailboat. The wingsail airfoil both single and two-element sail, and a cloth sail were investigated to determine the configuration that would provide the most thrust.

THIS PAGE INTENTIONALLY LEFT BLANK

II. BACKGROUND

The study of aerodynamics in sailing has traditionally been very challenging due to the dynamic environment of a sailboat. The design of sails prior to the 1960s was primarily based on experience and knowledge passed on from generation to generation. The 1960s saw the introduction of the first inviscid fluid solutions at the Massachusetts Institute of Technology [5]. Shortly after in the 1970s, Arvel Gentry from the Boeing Company began applying CFD techniques to investigate mainsail and jib interactions [5]. Beginning in the 1990s, computing power began to increase and became much more affordable. CFD computations were no longer just reserved for expensive supercomputers owned by NASA, the Department of Defense and aerospace engineering firms, but became a viable option to use in desktop form. Consequently, the America's Cup competition began to see the widespread application of RANS based CFD codes to improve sail designs. These codes were verified using experimental data and proved instrumental to driving the rapid increase in efficiency of the America's Cup sail designs.

The sailing community faces many challenges in accurately modeling the airflow over a sail due to a cloth sail's non-rigid nature. Challenges included modeling turbulent, laminar, separated, and reattached flow. Furthermore, cloth sails are difficult to model due to their sensitivity to trim settings. If a sail is not properly trimmed it can cause luffing, a state where the flow separates from the sail decreasing the efficiency of the sail significantly. Accurately modeling non-ideal trimming of a cloth sail using CFD is very difficult, however, RANS based codes proved useful in modeling separated flow across a perfectly trimmed sail. These codes were used to study both downwind and upwind sail configurations.

Various turbulence models have been used in CFD solutions to sail aerodynamics problems. In a study conducted by Collie, Gerritsen, and Jackson in 2001, they determined that a shear stress transport turbulence model most closely characterized the flow behavior over a sail [6]. Today the America's Cup is seeing sailboat speeds they would have thought impossible just 10 to 20 years earlier due impart to CFD research.

A. MOBILE OFFSHORE ENERGY PLATFORM CONCEPT

The rise in carbon emissions and the depletion of fossil fuels have created a need to investigate a reliable source for renewable energy [1]. The largely untapped energy of the oceans' winds is one potential source. Current resources use stationary off-shore wind turbines. Their technology is well developed, but being stationary makes these platforms dependent on the local wind. These platforms, therefore, produce very little energy during periods of low wind. Additionally, moorings or anchors are used for these platforms accounting for up to 20 percent of the cost of establishing a floating wind platform [1]. A mobile platform could follow the strongest winds in the ocean and store energy using batteries or compressed hydrogen [1]. Energy can be delivered directly to the cost avoiding costly infrastructure required by stationary platforms. The power of the winds over the oceans far exceeds the available offshore or inland wind power [1]. Tapping into the oceans' winds offers the potential to solve the world's energy needs in a renewable and sustainable way.

The proposed vehicle for this mobile platform is a sailing ship. The design requires the incorporation of a vessel, turbine, generator, desalinator, electrolyzer, compressor, and hydrogen tank [1]. The technology required to create an autonomous sailing vessel is already available. The challenge comes from the integration of all these parts.

Additional research in this subject area investigated the use of sails on engine-driven transportation ships. The use of sails on these transportation ships offers up to an 8.3 percent gain in efficiency [7]. Since most large trading ships today are propelled by diesel engines introducing sails on these vessels offers cost savings by reducing fuel consumption [7].

The mobile energy platform and transportation ships with sails use the mostly untapped energy of the oceans' winds. A correct application of currently available technology could open up a viable renewable energy resource.

B. CFD APPLICATION TO SAILS: A GENERAL OVERVIEW

For most of sailing's history the design of the sail was accomplished through knowledge passed down from generation to generation and experimentation. As mentioned

it wasn't until the 1960s when the introduction of numerical analysis to solve fluid dynamics problems offered potential for a better understanding of the flow. The scarcity and cost of high powered computers to conduct numerical analysis made the application of CFD to sailing few and far between. The emergence of the Navier-Stokes codes allowing for viscous flow calculations in the 1990s triggered a wave of research into sail aerodynamics [8]. The cost of computing power had decreased significantly as well, making CFD research available to a much larger group of people.

The sail aerodynamics problem is extremely dynamic with many variables. A traditional cloth sail seen on most recreational sailboats is constantly changing shape as it is trimmed. The shape of the sail provides the potential for laminar, turbulent, separated, and reattached flow occurring simultaneously across the chord length of the sail [5]. The introduction of Navier-Stokes codes offered a powerful tool to do this. As a result, the 1990s saw a rapid advance in sail design [8].

C. AERODYNAMICS OF SAILS RESEARCH PAST TO PRESENT

A primary driving force for sail aerodynamics research is the America's Cup. This annual sailboat race is an international competition where the winners walk away with fame and fortune. Unfortunately, most of the research done in this realm is proprietary. However, there are many research universities releasing information in the study of sail aerodynamics that investigate the America's Cup designs. The following sections list a few of the studies completed that are most applicable to this research project.

In 1989, Wilkinson published research on two-dimensional mast and sail geometries [9]. He detailed the pressure coefficient distribution over two different sail forms and several different camber settings. The radius of the leading edge, acting as the mast was varied as well. Wilkinson identified three distinct regions of flow over a sail. The first was a region of acceleration past the stagnation point around the mast of the sail. In this region the boundary layer was laminar. Region two was the area past the mast where the flow began to separate. Region three saw an instability of the boundary layer following the reattachment of the flow around the sail triggering a transition to turbulent flow. The

flow across the rest of the sail slowly lost energy against the adverse pressure gradient. Eventually, the flow would lose all its energy and separate.

A study conducted in 2006 by Amini et. al compared the advantages of rigid and cloth sails using CFD and experimentation [10]. This study took an angle of attack (AoA) sweep, and compared the velocities produced by the cloth and rigid airfoil like sail. The cloth sail produced greater velocities across the all angles of attack.

Also, in 2006 a study was conducted investigating sail-like rigid wings using CFD and experimental results by Yoo and Kim [11]. These results found that two sails placed together produced more lift than those sails placed separately. The gap area between these sails was very important to the total lift and thrust produced.

In 2009, Paton and Morvan from the University of Nottingham studied the effect of the jib mainsail interaction [3]. This paper used CFD to visualize the effect a jib has on a mainsail, and to correctly explain the phenomena known as the, "slot" effect. Several main sail and jib variations were investigated.

In 2012 a thesis from the University of Madrid investigated the pressure coefficient and aerodynamic performance of two high-performance sails of an IMS class boat and a Transpac 52 Class mainsail [12]. This study was conducted using two commercially available CFD codes. It identified weaknesses in CFD codes that were not specifically developed to investigate the flow fields over sails.

At the Northwestern Polytechnical University of Xi'an China in 2016, Cao et al., investigated the effect of oscillating an airfoil using NACA 0006 modified to a tadpole shape [13]. This study of several slightly different airfoil shapes found that the rate of oscillation had a far greater effect on performance than the airfoil shape modifications.

D. RESEARCH PAPERS USED FOR CFX MODEL VALIDATION

In order to validate the aerodynamic coefficient produced by CFD a test case for comparison was run for each type of airfoil.

The single element airfoil case was easiest to replicate and compare data. The *Theory of Wing Sections* by Abbott and Von Doenhoff provided an experimentally

produced lift curve and drag polar for comparison [14]. Additionally, a previous Naval Postgraduate School thesis, “Computational Investigations of NACA 0012 Airfoil in Low Reynolds Number Flows” by Lisa Nowak provided skin friction coefficients for comparison [15].

Validating the two-element airfoil test case proved more difficult. A test case in the “The Application of Computation Fluid dynamics to Sails” by Arvel Gentry was replicated [16]. The test case detailed the pressure coefficient across the two-element airfoil. This pressure coefficient was reproduced for model validation.

Finally, the cloth airfoil was validated using a thesis produced by Matthew Avila at the Naval Postgraduate School [8]. Avila’s thesis detailed several different cloth airfoils used by wind surfers. The geometry and results were replicated from this thesis to validate the model.

THIS PAGE INTENTIONALLY LEFT BLANK

III. EXPERIMENTAL PROCEDURE

Three types of airfoils, single-element, two-element, and cloth sail airfoils were tested to determine the best design for the hydroelectric sailboat. To validate the flow solution for each airfoil, a test case was run, and compared to either experimental or CFD data found in the literature.

A. FUNDAMENTAL ASSUMPTIONS

Since the aspect ratio of sailboats tends to be very high the three-dimensional effects of the wing were neglected and all tests were conducted assuming two-dimensional flow. All flows were below Mach 0.3 and thus treated as incompressible. At these conditions heat transfer was considered negligible.

B. CFD SOLVER AND THEORY

ANSYS CFX was used as the CFD program to numerically solve for aerodynamic coefficients over the single, two-element, and cloth sail airfoils.

1. CFX Governing Equations

CFX uses the conservative form of the unsteady Navier-Stokes equations to solve fluid flows. All equations listed in this Section were obtained from source [17]. Equations (1) is the instantaneous continuity equation.

$$\frac{\partial \rho}{\partial t} + \nabla \bullet \left(\rho U \right) = 0 \tag{1}$$

Equation (2) is the instantaneous momentum equation with the stress tensor, τ, defined in Equation (3).

$$\frac{\partial \left(\rho U \right)}{\partial t} + \nabla \bullet \left(\rho U \otimes U \right) = -\nabla p + \nabla \bullet \tau + S_M \tag{2}$$

$$\tau = \mu \left(\nabla U + \left(\nabla U \right)^T - \frac{2}{3} \delta \nabla \bullet U \right) \tag{3}$$

Equation (4) is the instantaneous total energy equation where h_{tot} is given by Equation (5)
.

$$\frac{\partial\left(\rho h_{tot}\right)}{\partial t}-\frac{\partial p}{\partial t}+\nabla\bullet\left(\rho U h_{tot}\right)=\nabla\bullet\left(\lambda\nabla T\right)+\nabla\bullet\left(U\bullet\tau\right)+U\bullet S_M+S_E \tag{4}$$

$$h_{tot}=h+\frac{1}{2}U^2 \tag{5}$$

Equations (1), (2), and (4) are the transport equations used as the basis to solve fluid dynamics problems. Equations (6), (7), and (8) are incompressible gas equations of state required to create a closed form solution of the transport equations.

$$\rho=\rho_{spec} \tag{6}$$

$$dh=c_p dT+\frac{dp}{\rho} \tag{7}$$

$$c_p=c_p\left(T\right) \tag{8}$$

Density is calculated using the ideal gas law in Equation (9).

$$\rho=\frac{p}{R_o T} \tag{9}$$

2. Modeling Turbulence

The Navier-Stokes equations are capable of solving both laminar and turbulent flows. However, to directly solve for turbulent flow the numerical solution would be extremely complex and take years of super-computing power that is currently unavailable [17]. Since solving for turbulence using the Navier Stokes Equations was not feasible, turbulence models were developed to approximate turbulent flow behavior. Turbulence models use averaged and fluctuating quantities of the Navier-Stokes equations to create Reynolds Averaged Navier-Stokes (RANS) equations [17]. These RANS based equations are the basis for many CFD turbulence models.

3. Turbulence Model: Shear Stress Transport (SST) with Gamma-Theta transition

Shear stress transport (SST) is based on the k-omega turbulence model [17]. SST is able to account for the shear stress movement throughout the flow, and yields a good prediction of flow separation in adverse pressure gradients [17]. The Gamma-Theta transition model was used to predict the transition from a laminar to a turbulent boundary layer.

C. SINGLE ELEMENT AIRFOIL ANALYSIS PROBLEM SET-UP

NACA 0012 single element airfoil analysis was completed first as it was the simplest problem of the three airfoils, and had the most readily available experimental data for comparison. The model was validated by comparing experimental data found in Abbott and Von Doenhoff (reference [14]) and CFD data found in Nowak's thesis [15].

1. SolidWorks Model Geometry

Figure 4 displays the NACA 0012 airfoil geometry drawn in SolidWorks. The geometry was drawn using a set of coordinates generated using the MATLAB script in Appendix C. NACA Airfoil Coordinate Generation Code. The chord was 1 meter and the thickest point of the airfoil was 0.12 meters.

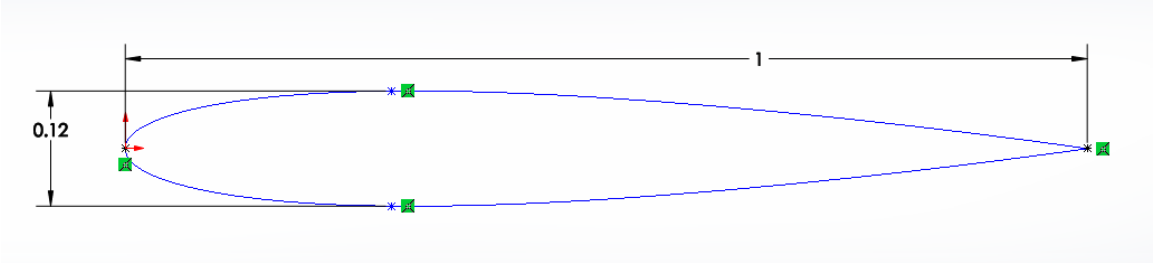

Figure 4. NACA 0012 airfoil with dimensions in meters

A box was drawn around the airfoil and then extruded 2 millimeters in order to create a volume to solve the fluid flow within CFX. The box drawn around the airfoil is shown in Figure 5.

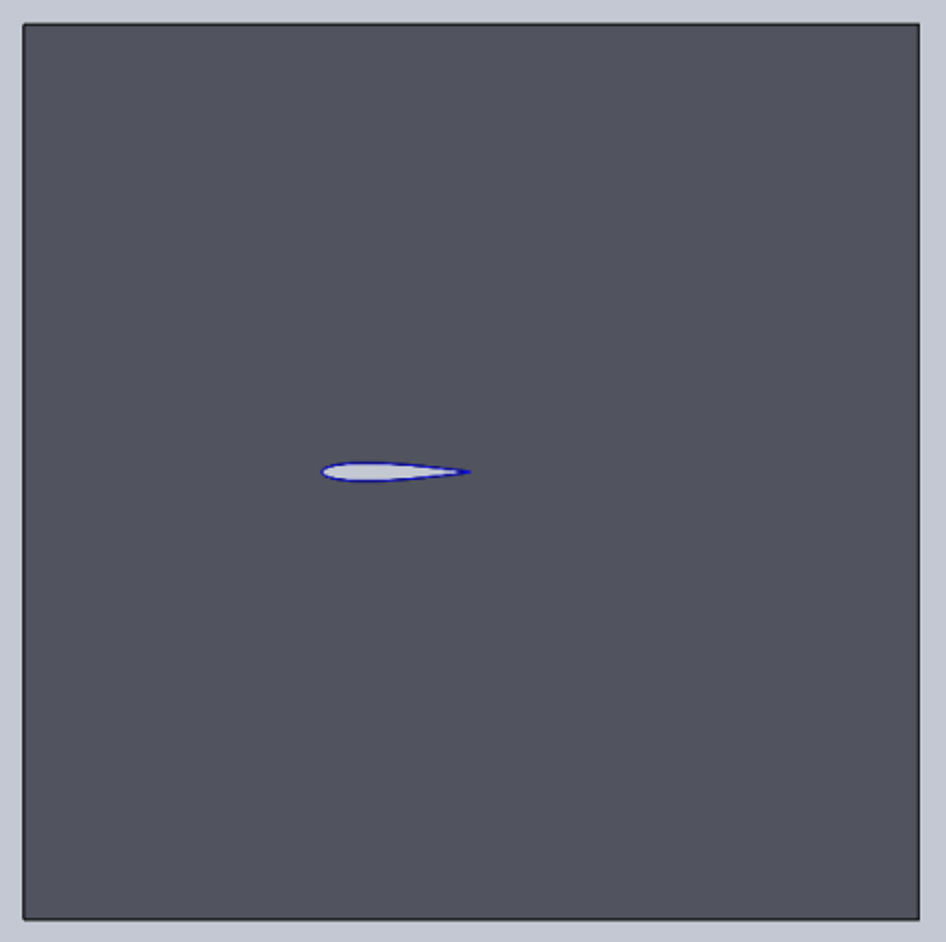

Figure 5. Solution volume drawn around airfoil

2. Meshing

Creating a mesh fine enough around the airfoil to successfully resolve the boundary layer was key to obtaining an accurate C_d and C_f. C_l can be resolved using much simpler methods such as a panel code, therefore it was not considered as a good indicator of the accuracy of the results.

a. Reynolds Number of Three Million Mesh

To obtain a detailed mesh around the airfoil an edge sizing and inflation layer were added. The inflation layer was set to 51 layers across the airfoils face with the maximum thickness set to 5e-3 meters and a growth rate of 1.1. The edge sizing around the airfoil was set to 4000 divisions with a bias factor of 4.0. Table 1 displays the mesh sizing metrics.

Table 1. NACA0012 mesh size data

Mesh Category	Number
Nodes	852,542
Elements	1,412,498

Figure 6 displays the entire mesh used to calculated fluid solutions for the NACA 0012 airfoil. Figure 7 displays a zoomed in look at the inflation layer surrounding the entire airfoil.

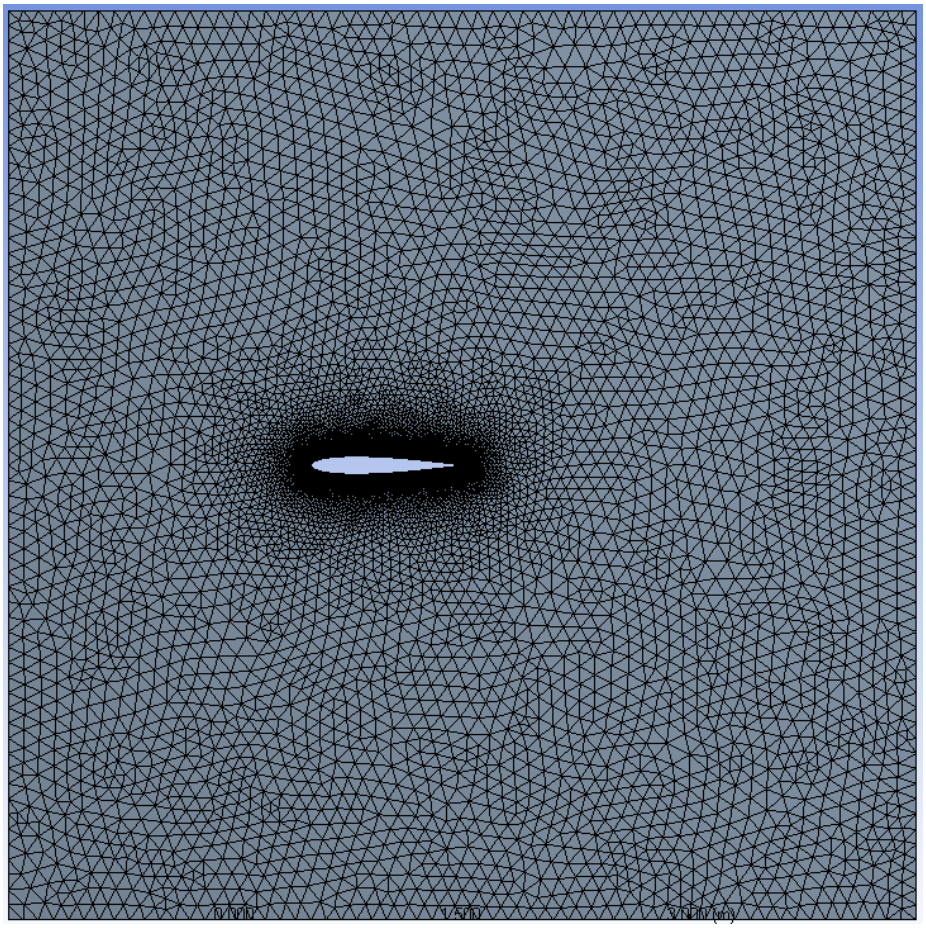

Figure 6. NACA0012 solution mesh for Re 3 million

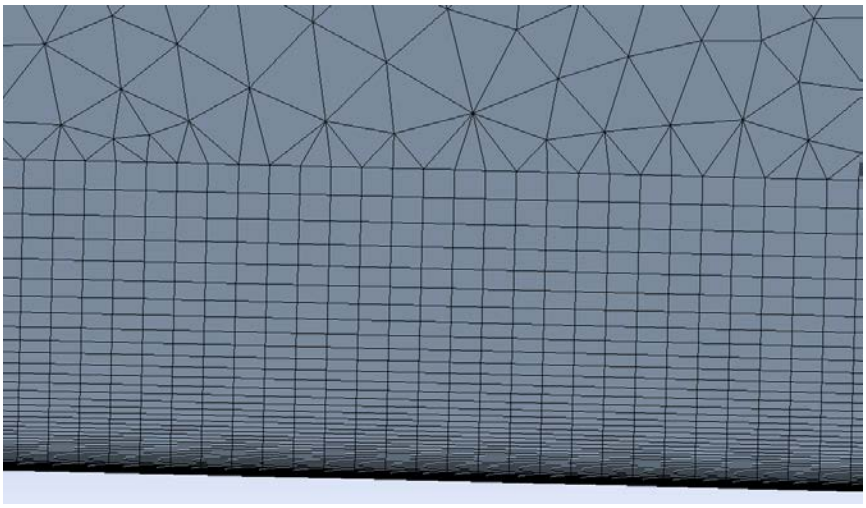

Figure 7. NACA 0012 inflation layer surrounding airfoil for Re 3 million

b. Reynolds Number One Million Mesh

It was found that the mesh used to obtain a solution for a Reynolds number of three million for the NACA 0012 yielded a non-physical answer at a Reynolds number of one million. A mesh using the same technique outlined for the two-element airfoil was used. Refer to Appendix A. geometry and mesh creation guide for the detailed procedure of how the mesh was created.

An edge sizing, inflation layer, and sweep method were used to create the one million Reynolds number mesh. An inflation layer was placed on the front face of the geometry with the first layer thickness of 1e-6 meters. A total of 71 layers were placed at a growth rate of 1.1 starting at the airfoils' edge. An edge sizing dividing the airfoils into 1000 segments was then added. Finally a sweep method was used to copy the mesh created on the front face throughout the entire geometry. Table 2 displays the total number of nodes and elements in the single element one million Reynolds number mesh.

Table 2. Reynolds number one million single element airfoil mesh statistics

Mesh Category	Number
Nodes	182,736
Elements	110,528

Figure 8 displays the overall mesh used to calculate the one million Reynolds number flow solution. Figure 9 displays a zoomed in look at the inflation layers used to resolve the boundary layer of the NACA 0012 Reynolds number one million fluid flow problem.

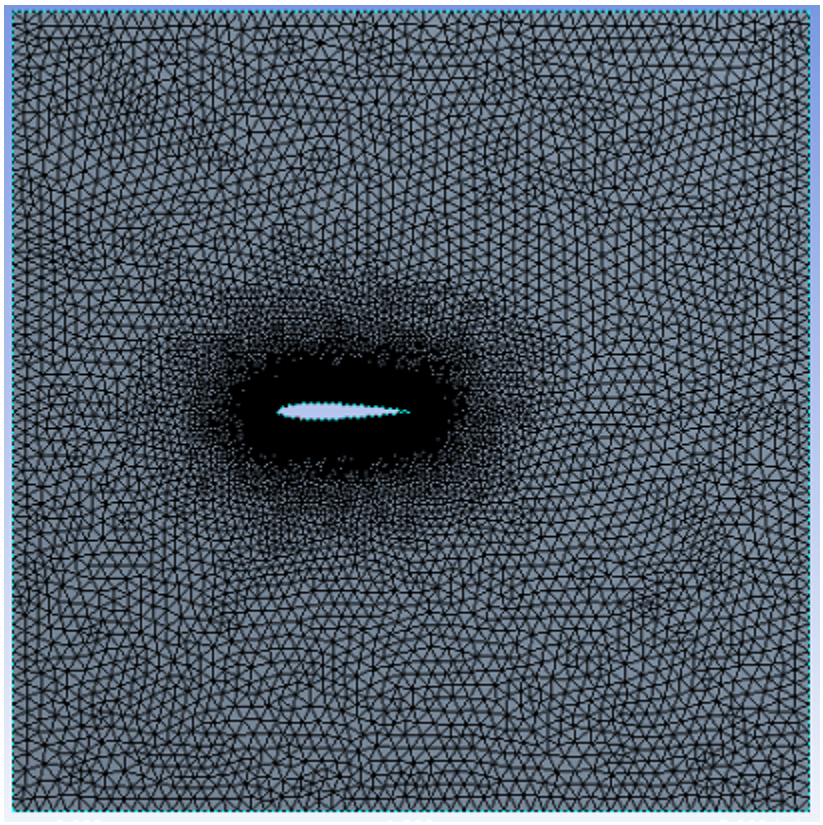

Figure 8. NACA 0012 solution mesh for Reynolds number one million

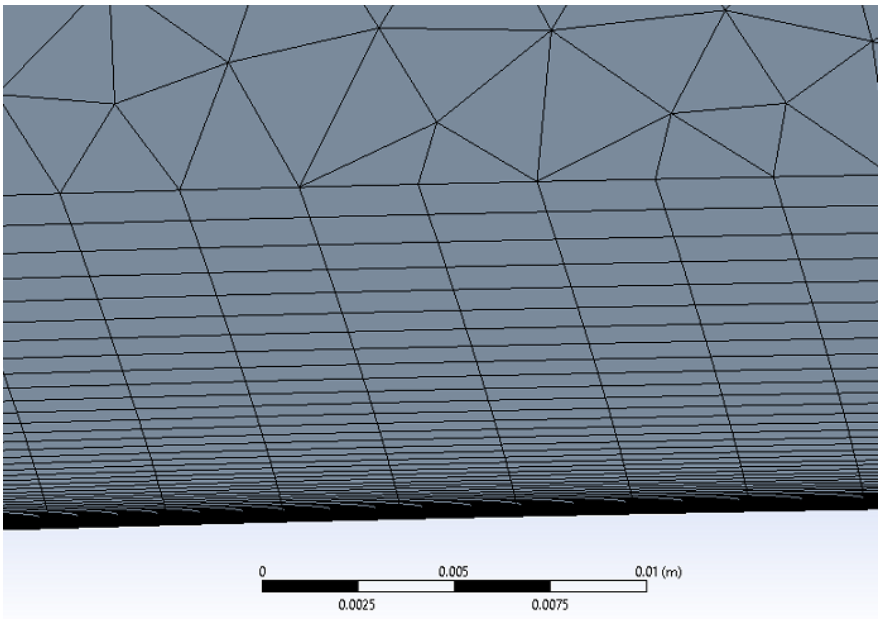

Figure 9. NACA 0012 inflation layer surrounding airfoil for Reynolds number one million

3. Solution Parameters

The reference pressure was set to one atmosphere, and the fluid was set to air at 25 degrees Celsius. Since the flow velocities investigated were all subsonic and below Mach 0.3 the flow was assumed to be isothermal. The turbulence model used was SST with the gamma-theta model for transition (described in section B.3). Refer to Figure 10 for the titles of the geometry used to set-up the solution. The bottom and inlet side of the geometry were set as inlet conditions in the initial set-up. The AoA was varied by change the x and y velocity components to create the desired vector of air at both the inlet and bottom of the geometry.

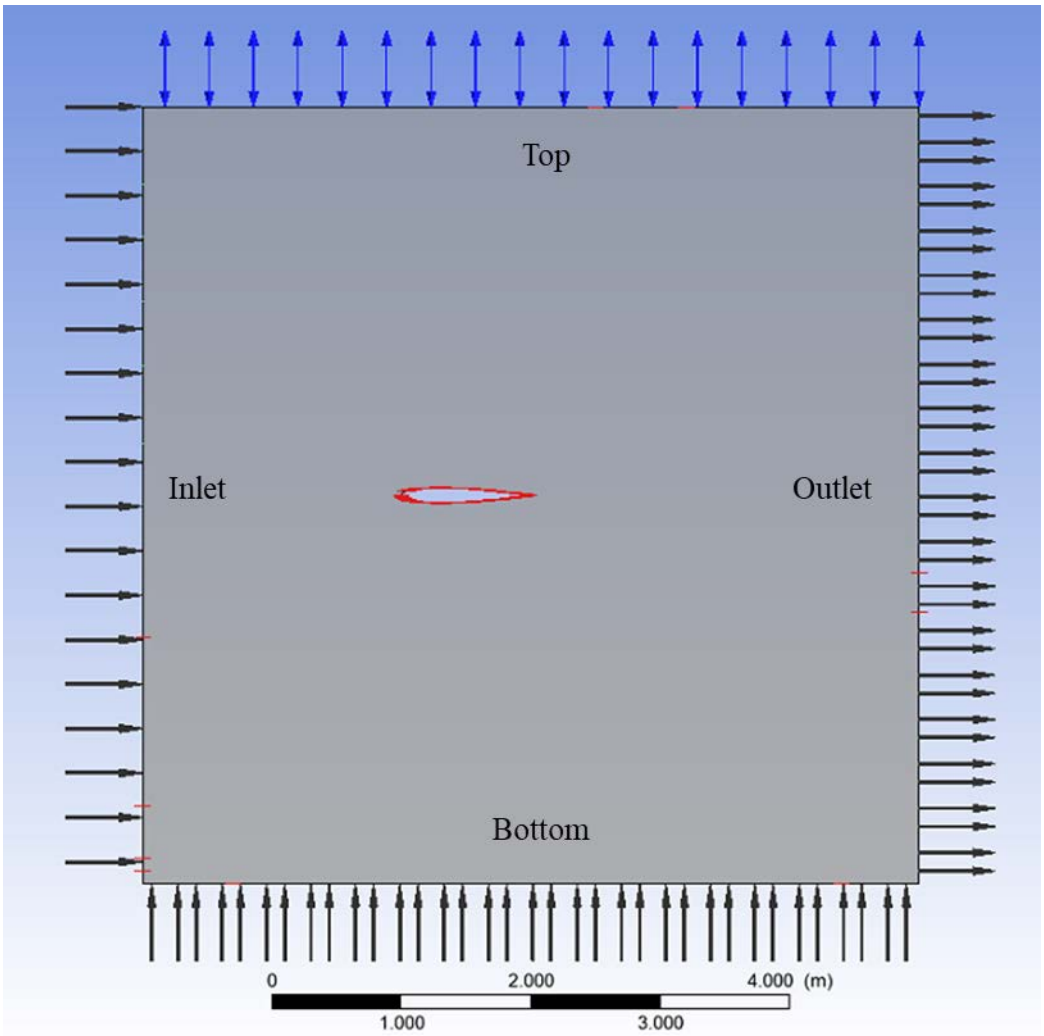

Figure 10. NACA 0012 solution set-up

The free stream velocity was determined to be 54.86 meters per second based on a desired Reynolds number of three million. A Reynolds number of three million was chosen to compare with results found in Abbott and Von Doenhoff [14]. The angle of attack was changed by changing the inlet velocity components in x and y direction at both the bottom and inlet to achieve angles of attack between negative four and positive eighteen degrees.

The airfoil boundary was set as a no-slip wall, and the top boundary was set as an entrainment with zero relative pressure. The front and back planes were set as symmetry boundaries to produce a two-dimensional solution. The basic solver control settings were set to a maximum of 700 iterations with an RMS value of 1e-11.

The comparison single element test case was run at a Reynolds number of one million.

D. TWO ELEMENT AIRFOIL ANALYSIS PROBLEM SET-UP

The two-element airfoil problem required two different geometries to first validate the model and then accurately compare to the cloth sail and single element airfoils. The test case was taken from "The applications of Computational Fluid Dynamics to Sails" by Arvel Gentry (see reference [16]). A repeat analysis of the two-element airfoil design documented in the journal article was conducted. After verifying the results with the journal article, a similar mesh and settings were used to produce the two-element airfoil comparison test case. For the comparison test case two NACA 0012 airfoils of a chord length 0.5 meters were used. This set-up most accurately replicated the flow over the 1-meter chord of the single element and cloth sail airfoils.

1. SolidWorks Model Geometry

Figure 11 displays the Gentry test case geometry. The article neglected to name the type of airfoil used in the analysis. Consequently, to determine the type of airfoil used, the airfoil geometries were measured from the graphic provided in the article and comparable NACA airfoils were used to model the flow. The front airfoil used a NACA 0020 with a chord and max camber of 1 meter and 0.2 meters respectively. The aft airfoil displayed a chord and max camber of 1 meter and 0.07 meters respectively. The aft airfoil was deflected 20˚ degrees. The coordinates used to draw these airfoils were generated using the code in Appendix C. NACA Airfoil Coordinate Generation Code.

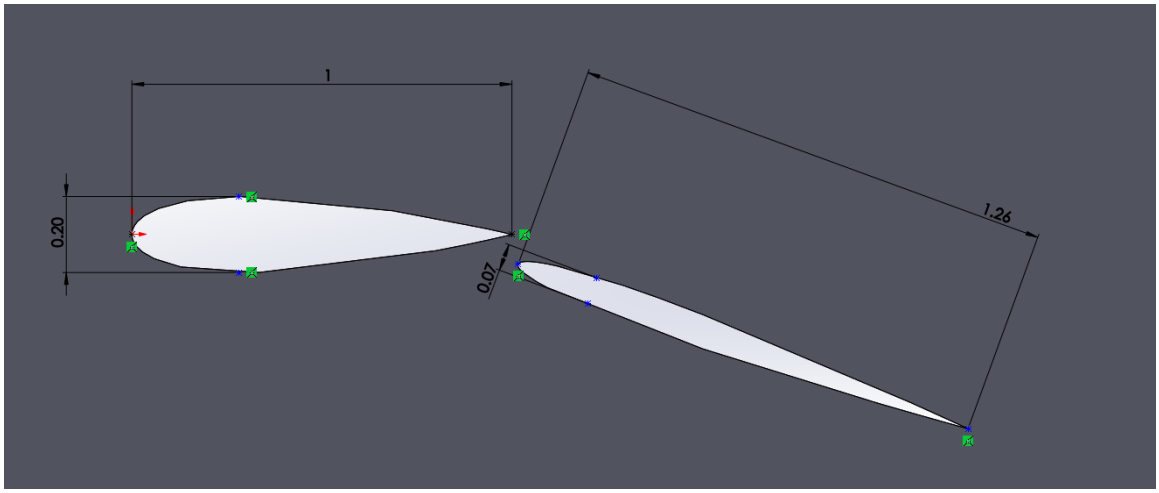

Figure 11. NACA 0020 positioned in front of a NACA 0007 used in the Gentry test case

Figure 12 displays the two element airfoil used to compare with the single element and cloth sail airfoils. A NACA 0012 airfoil was used in both the front and aft position of the airfoil with a chord length 0.5 meters respectively, and max camber of 0.06 meters. The aft airfoil was deflected 15˚ degrees with a pivot point located at 80 percent of the front airfoil's chord.

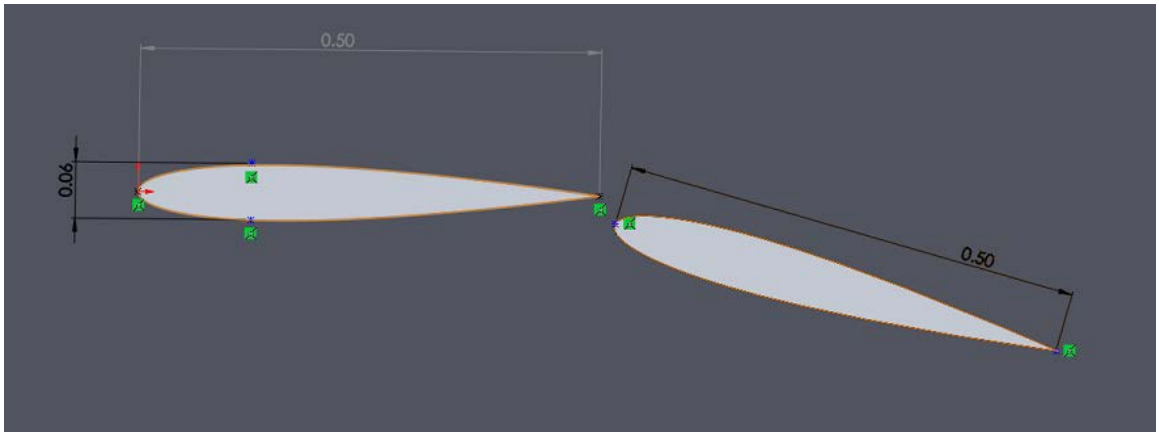

Figure 12. Two-element airfoil with NACA 0012 used in both segments for comparison to cloth sail and single element airfoils

2. Meshing

The Gentry test case was used to validate the results of the CFX fluid flow model. The Gentry case gave the pressure coefficient for the two-dimensional airfoil geometry given in Figure 11. The meshing parameters and fluid flow solution set-up used to successfully solve the Gentry test case were mirrored on the two-element airfoil test case.

a. Gentry Test Case Mesh

An edge sizing, inflation layer, and sweep method were used to create the Gentry test case mesh. An inflation layer was placed on the front face of the geometry with the first layer thickness of 1e-6 meters. A total of 51 layers were placed at a growth rate of 1.1 starting at the airfoils' edge. An edge sizing dividing the airfoils into 4000 segments was then added. Finally a sweep method was used to copy the mesh created on the front face throughout the entire geometry.

Table 3 gives the mesh size of Gentry test case.

Table 3. Two element Gentry test case mesh size

Mesh Category	Number
Nodes	1056992
Elements	640462

Figure 13 displays the Gentry test case solution mesh. Figure 14 displays the Gentry test case inflation layer of the solution mesh.

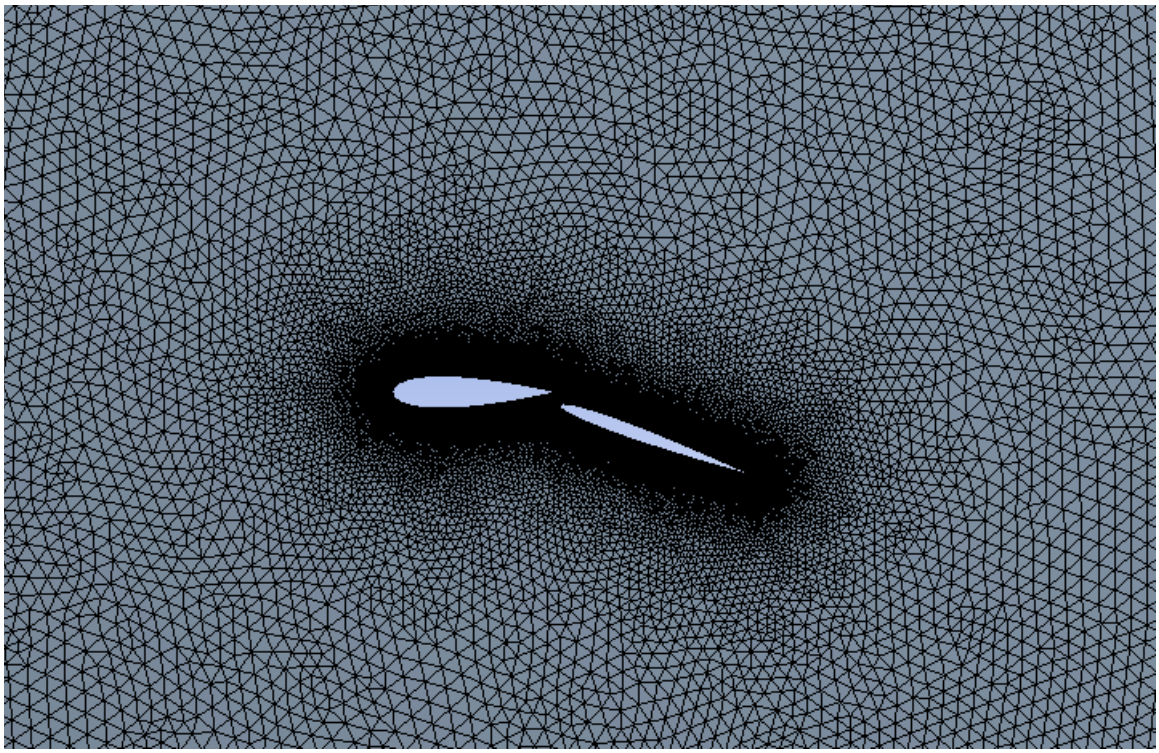

Figure 13. Two element Gentry test case solution mesh

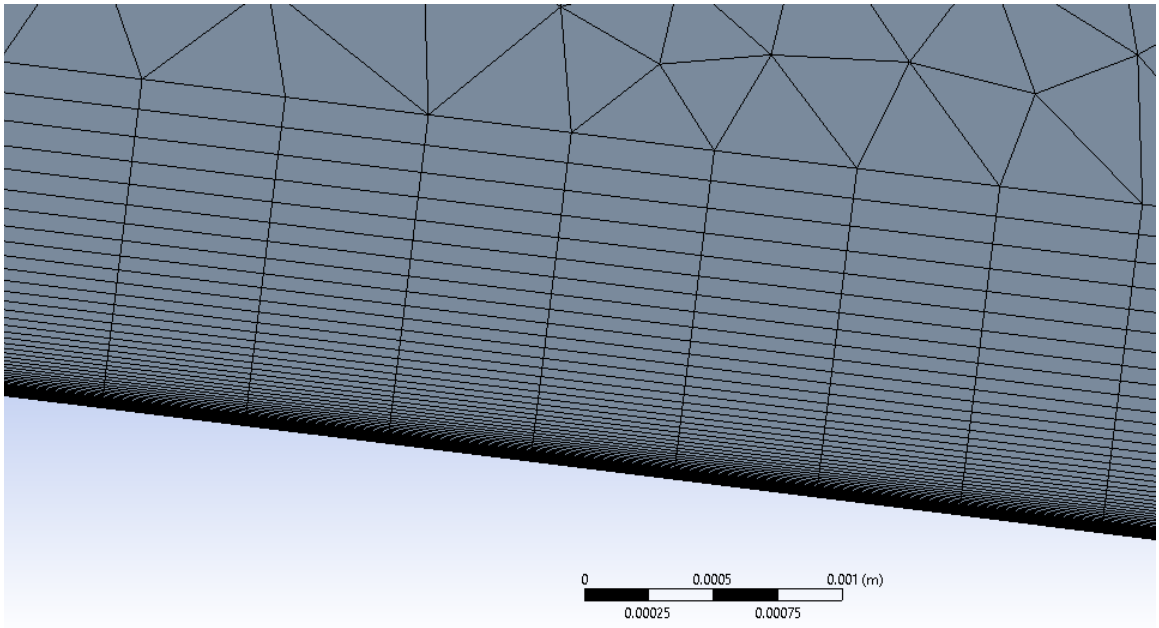

Figure 14. Inflation layer of two-element Gentry test case

b. Two Element Airfoil Comparison Test Case

The same procedures used in the Arvel Gentry test case were used to create the two-element airfoil test case for comparison. An inflation layer was inserted along the airfoils edge with the first layer thickness defined as 1e-6 meters. A growth rate of 1.1 was used, and a total of 71 inflation layers were inserted. An edge sizing was inserted with dividing each airfoil edge into 1500 segments.

Table 4 displays the two-element comparison test case mesh size.

Table 4. Two-element comparison test case mesh size

Mesh Category	Number
Nodes	503142
Elements	286604

Figure 15 displays the mesh used to solve the fluid flow over the two-element airfoil comparison. Figure 16 displays the inflation layer inserted around the two-element airfoil comparison test case.

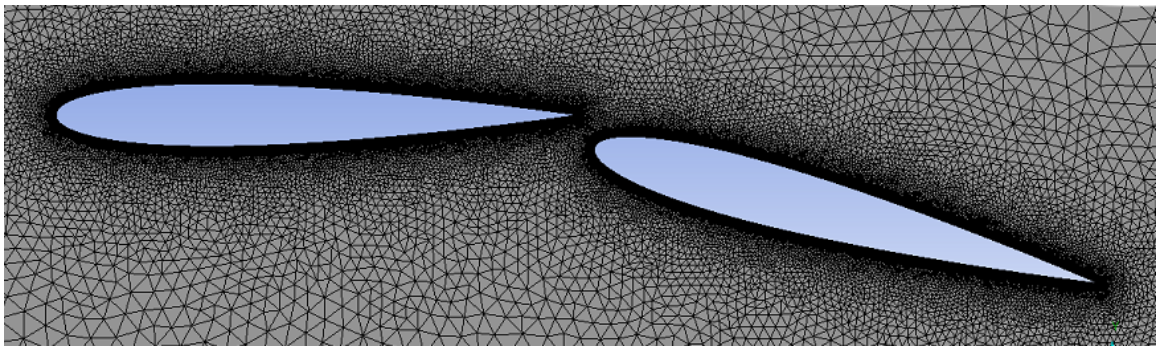

Figure 15. Two-element airfoil comparison test case mesh

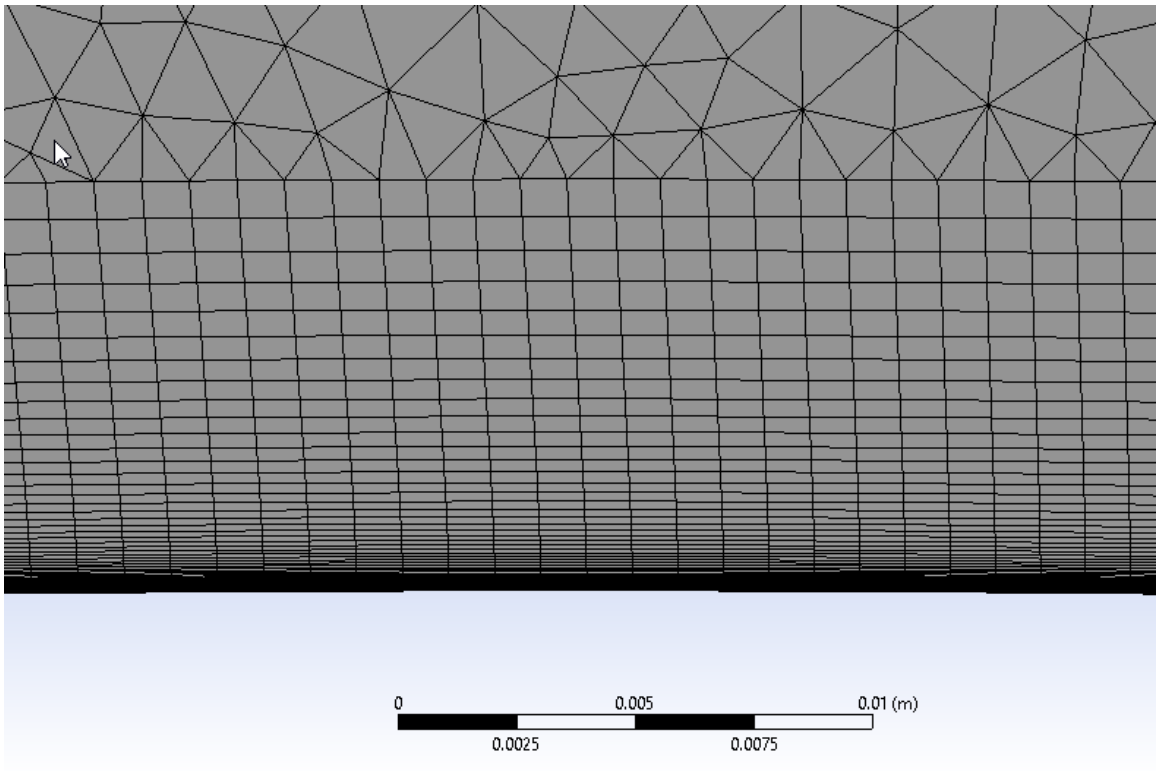

Figure 16. Inflation layer of two-element airfoil comparison test case

3. Solution Parameters

The Arvel Gentry test case was run at a Reynolds number of 800,000. This set the free stream velocity at 15.91 meters per second. The two-element comparison test case was run at a Reynolds number of one million. The model used the SST model with the gamma theta transition. The solution parameters and naming convention were the same in the two-element airfoil test case as they were in the single element test case.

E. CLOTH SAIL AIRFOIL ANALYSIS PROBLEM SET-UP

1. SolidWorks Model Geometry

The sail geometry displayed in Figure 17 was copied from a Naval Postgraduate School thesis from Matthew Avila [8]. The sail is 11.5 percent camber and one meter in chord length. In Solidworks an extruded cut of one millimeter wide and two millimeters in depth was made to define the sail inside the box of air.

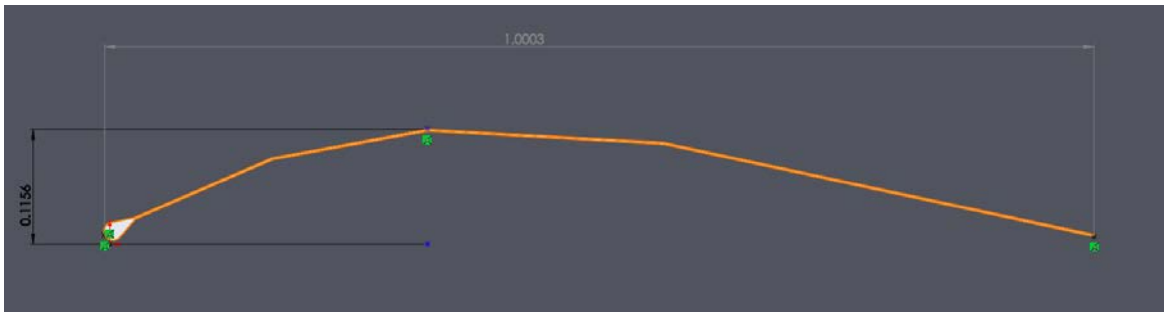

Figure 17. Cloth sail airfoil geometry. Source: [8].

2. Meshing

Creating a suitable mesh for the cloth sail proved to be more difficult than the single and two-element airfoils. An inflation layer was not able to be generated along the edge of the sail. The source of this difficulty is thought to be the thin cross section of the sail. An edge sizing of 1e-4 meters and sweep method were exclusively used. Table 5 displays the number of nodes and elements present in the mesh. Due to the lack of an inflation layer the boundary layer was not captured to the degree of accuracy for the sail airfoil as it was for the single and two-element airfoils.

Table 5. Cloth sail airfoil mesh size

Mesh Category	Number
Nodes	1785128
Elements	894344

Figure 18 displays the overall mesh around the cloth sail airfoil. Figure 19 displays a closer look at the cloth sail's edge sizing.

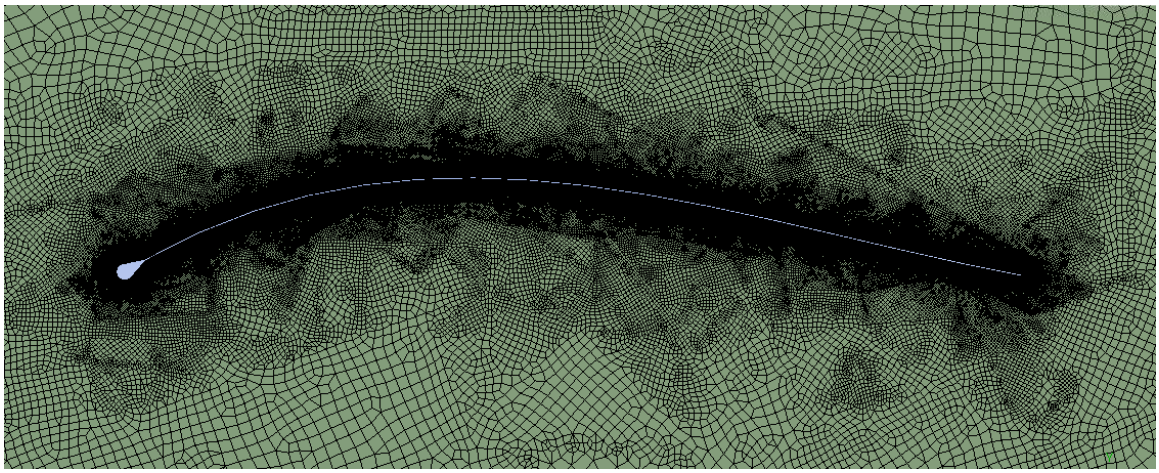

Figure 18. Cloth sail airfoil mesh

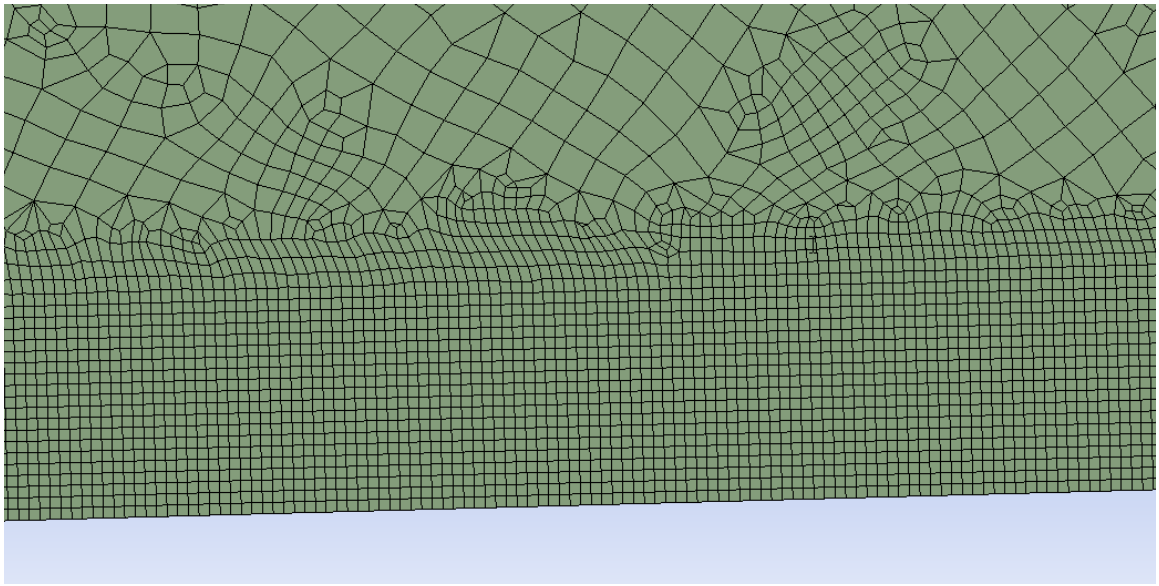

Figure 19. Cloth sail airfoil mesh edge sizing

3. Solution Parameters

The free stream velocity for the Avila test was 15.91 meters per second to obtain a Reynolds number of 800,000. The SST with gamma theta transition model was used along with the same set-up parameters outlined for the single and two-element airfoil tests. For the cloth sail the comparison was run at a Reynolds number of one million.

THIS PAGE INTENTIONALLY LEFT BLANK

IV. RESULTS

A. NACA 0012 CASE STUDY

1. Convergence and Yplus Values

For the single element airfoil a Yplus from 0.1 to 2 was achieved for all AoAs for a Reynolds number of one and three million. The boundary layer was effectively captured by the mesh used in the simulations.

Figure 20 displays the mass and momentum RMS convergence for a single element airfoil at 4˚ AoA Reynolds number of three million. Mass and momentum RMS values converged between 1e-4 and 1e-6.

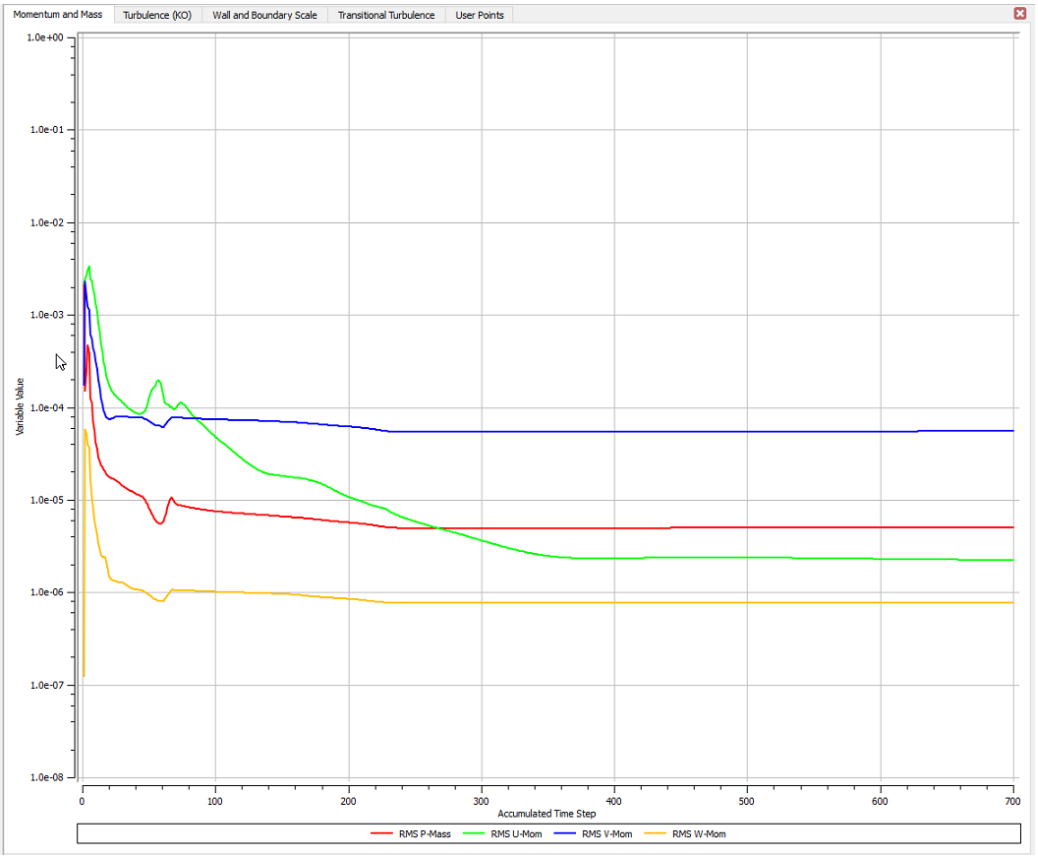

Figure 20. Mass and momentum convergence single element airfoil at AoA 4˚ Reynolds number 3 million

Figure 21 displays the convergence history for the one million Reynolds number run of the single element airfoil at a four-degree AoA. Mass and momentum RMS values converged between 1e-5 and 1e-7.

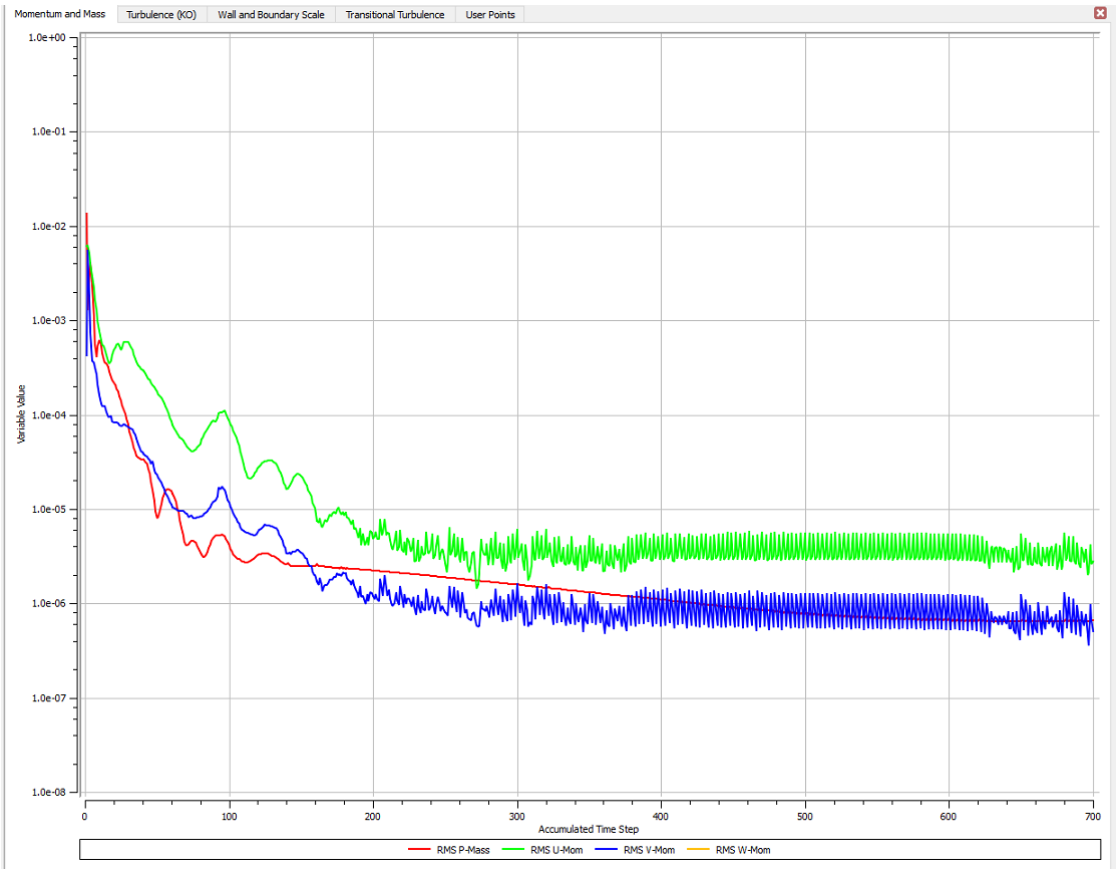

Figure 21. Mass and momentum convergence single element airfoil at AoA 4˚ Reynolds number 1 million

Similar convergence to that seen in Figure 20 and Figure 21for all other AoAs was observed.

2. Abbott and Von Doenhoff Result Comparison

The first test case ran was the single element airfoil at a Reynolds number of three million for comparison to Abbott and Von Doenhoff's *Theory of Wing Sections* [14]. The lift and drag coefficients were recorded for an AoA sweep from minus four to 20 degrees.

Figure 22 displays the lift coefficient versus AoA for a NACA 0012 airfoil comparing the CFD and experimental results. The simulation's lift coefficient agreement with experimental results was very good. This high degree of agreement was expected. Lift coefficient has been accurately predicted using far less advanced approaches such as a panel code.

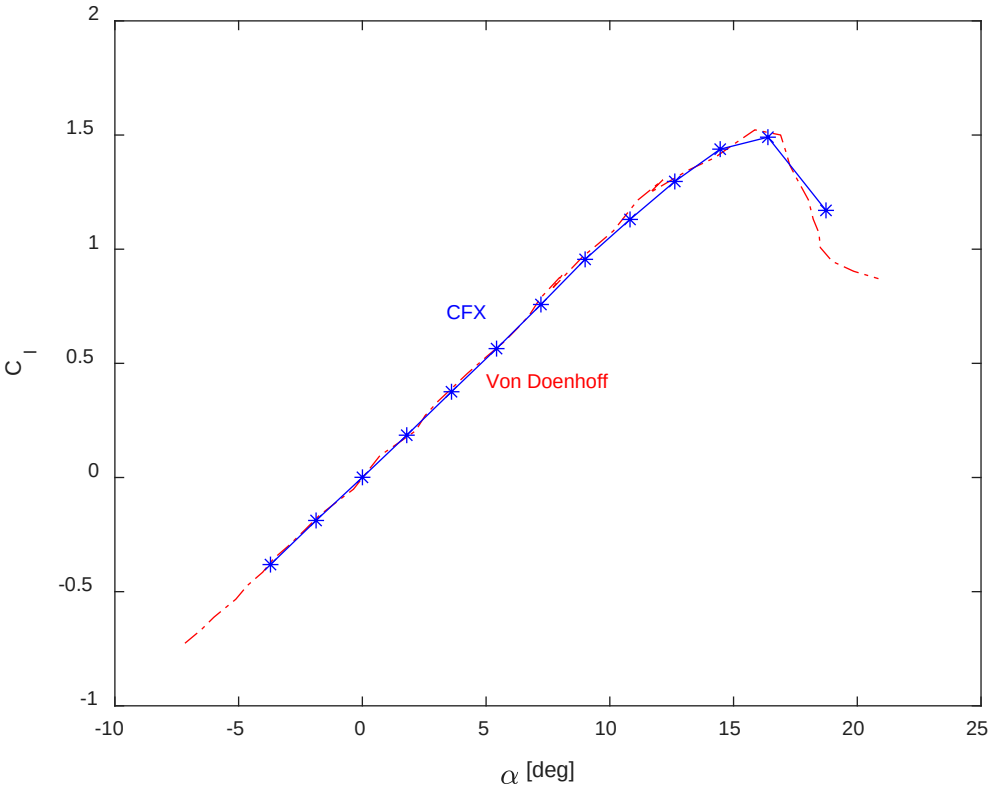

Figure 22. NACA 0012 CFX results compared to Abbott and Von Doenhoff experimental results

Figure 23 compares the CFD and Abbott and Von Doenhoff's experimental results by plotting drag coefficient versus lift coefficient. Predicting the drag of an airfoil is far more difficult than predicting the lift. AoA's minus four through six degrees showed remarkable agreement with experimental results. However, starting at an AoA of eight degrees and above CFD predicted a higher drag value than the experimental results.

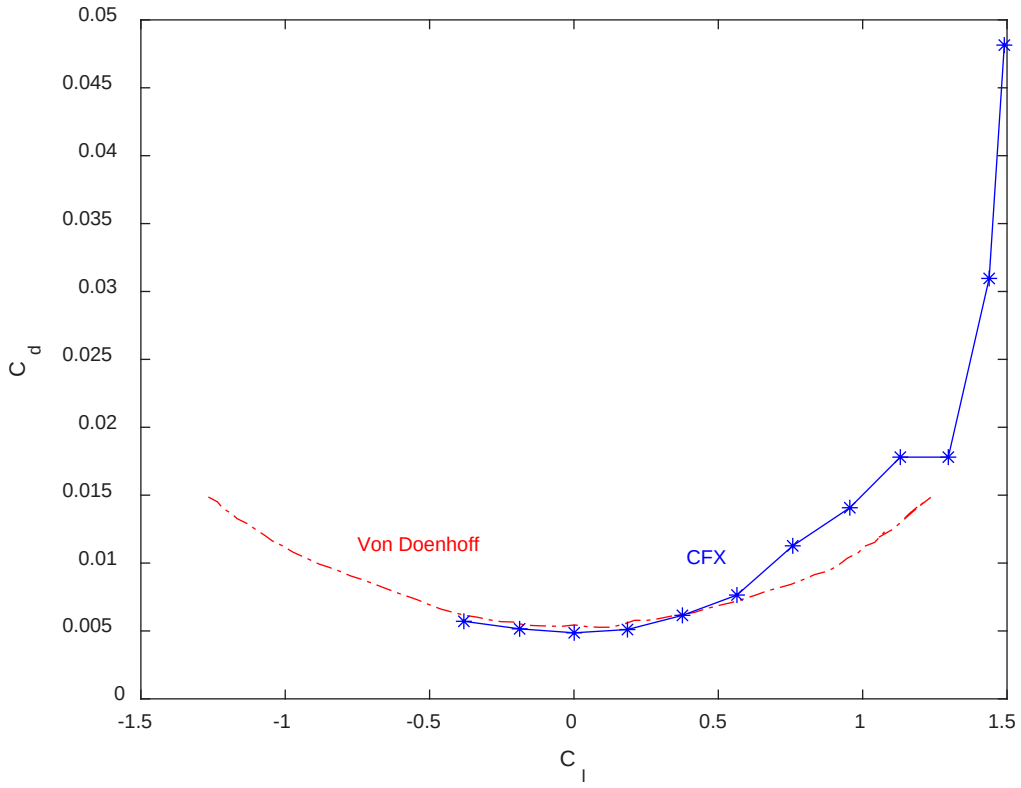

Figure 23. Comparison of CFX results and Abbott and Von Doenhoff

In order to determine the source of this error a closer look at the boundary layer along the suction side of the airfoil was conducted. Several observations were made. A separation bubble appeared at around AoA six degrees and persisted until stall at AoA of 18 degrees and flow separation occurred at the trailing edge at a 12 degree AoA.

3. Separation Bubble Investigation

Figure 24 displays the pressure coefficient versus the chord location along the NACA 0012 airfoil at an AoA of eight degrees at a Reynolds number of three million. The black circle indicates a sudden pressure increase on the suction surface which indicates the formation of a separation bubble.

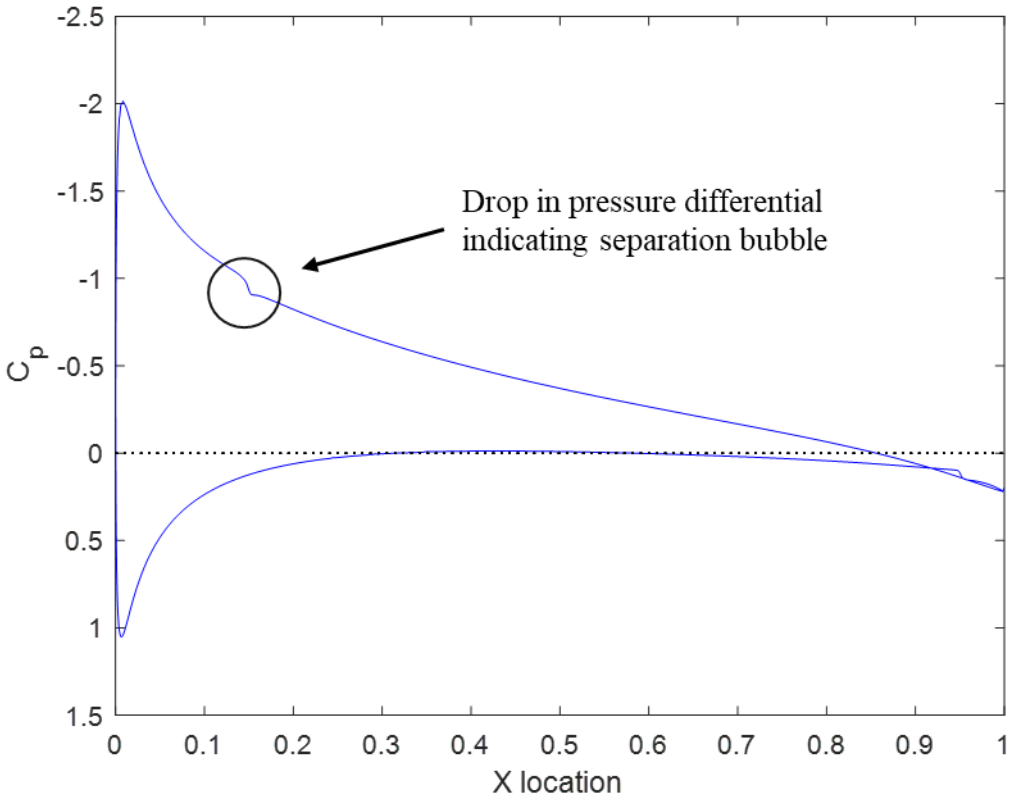

Figure 24. Pressure coefficient of AoA 8˚ Reynold number three million, Single element airfoil

In order to analyze the separation bubble in more detail three boundary layer profiles were taken at the start, middle, and end of the separation bubble at an eight degree AoA. Please refer to Appendix B. Boundary Layer Plot Technique cfd-post for the detailed procedure for how this was achieved.

Figure 25 displays the locations where the separation bubble boundary layer profiles were taken along with their location with respect to percent chord.

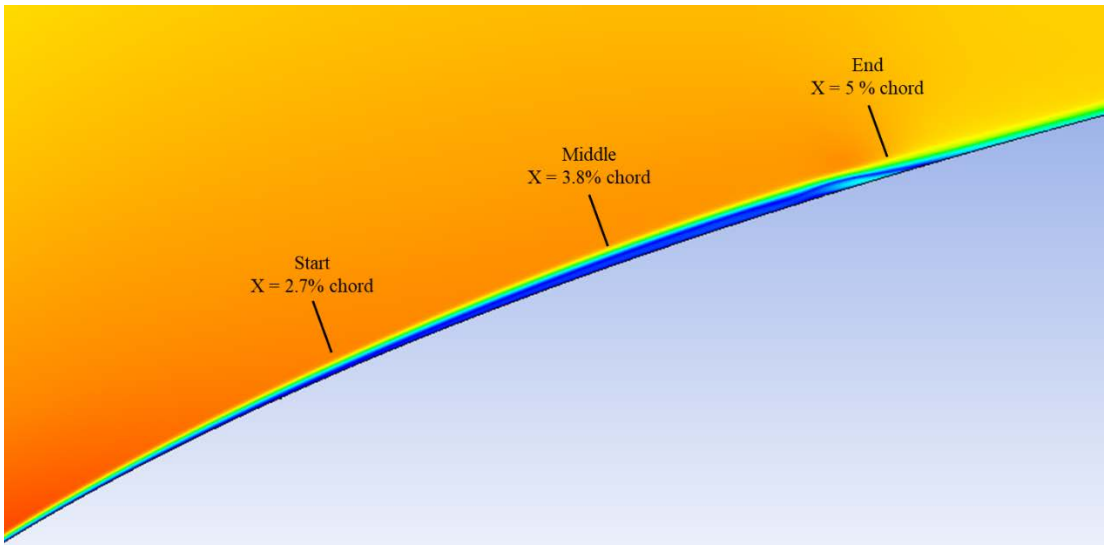

Figure 25. Start, middle, and end locations displayed in BL plot (Figure 26)

Figure 26 displays the boundary layer profiles at the start, middle, and end of the eight-degree AoA separation bubble. At the start of the bubble zero velocity begins to grow from the surface. The middle profile indicates a reversal and separation of the flow from 0 to 0.03 percent chord. Finally the end profile displays zero velocity from the surface to 0.01 percent chord length above the surface. Above 0.01 percent chord from the surface air flows in the positive direction showing reattachment of the flow. Figure 25 gives a more visual representation of this process. A blue color indicates zero velocity and possible flow separation. The green to yellow transition indicates the boundary layer with attached flow in the positive direction along the airfoil.

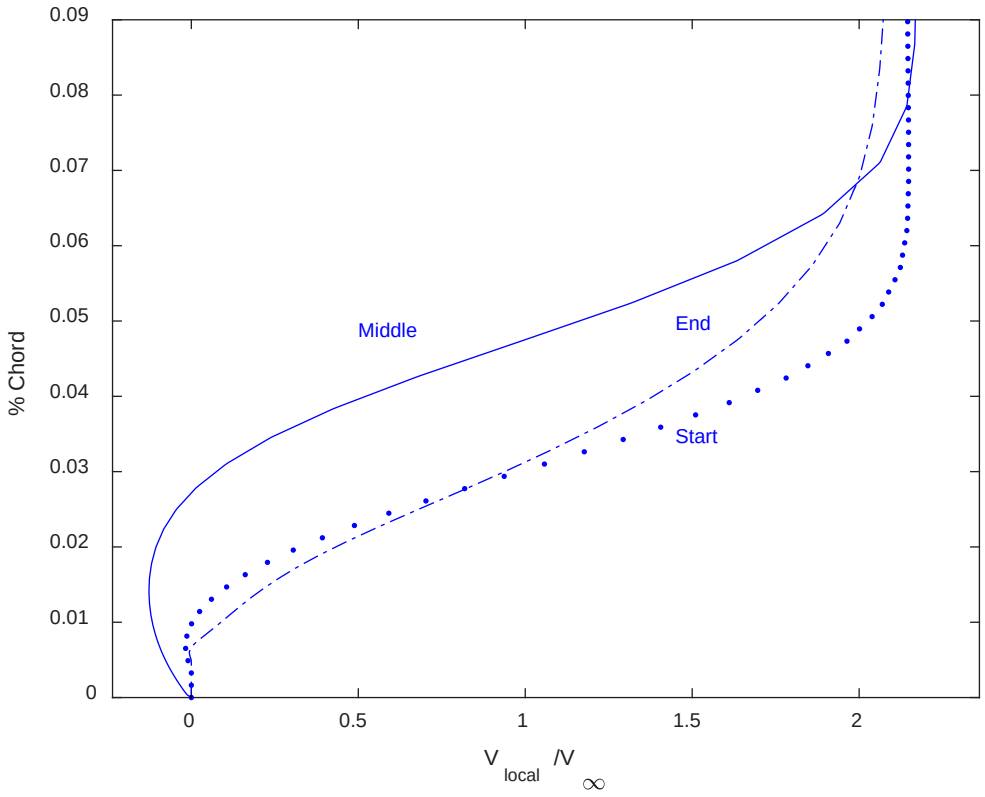

Figure 26. Separation Bubble, AoA 8˚, start, middle, and end, Re 3 Million

The separation bubble persisted from AoA six degrees through stall at AoA of 18 degrees. Figure 27 displays the NACA 0012 airfoil stalled at an AoA of 18 degrees. At 0.05 percent chord the separation bubble begins to cause flow separation. Due to the high AoA the flow is no longer able to reattach and total separation begins at 1.5 percent chord.

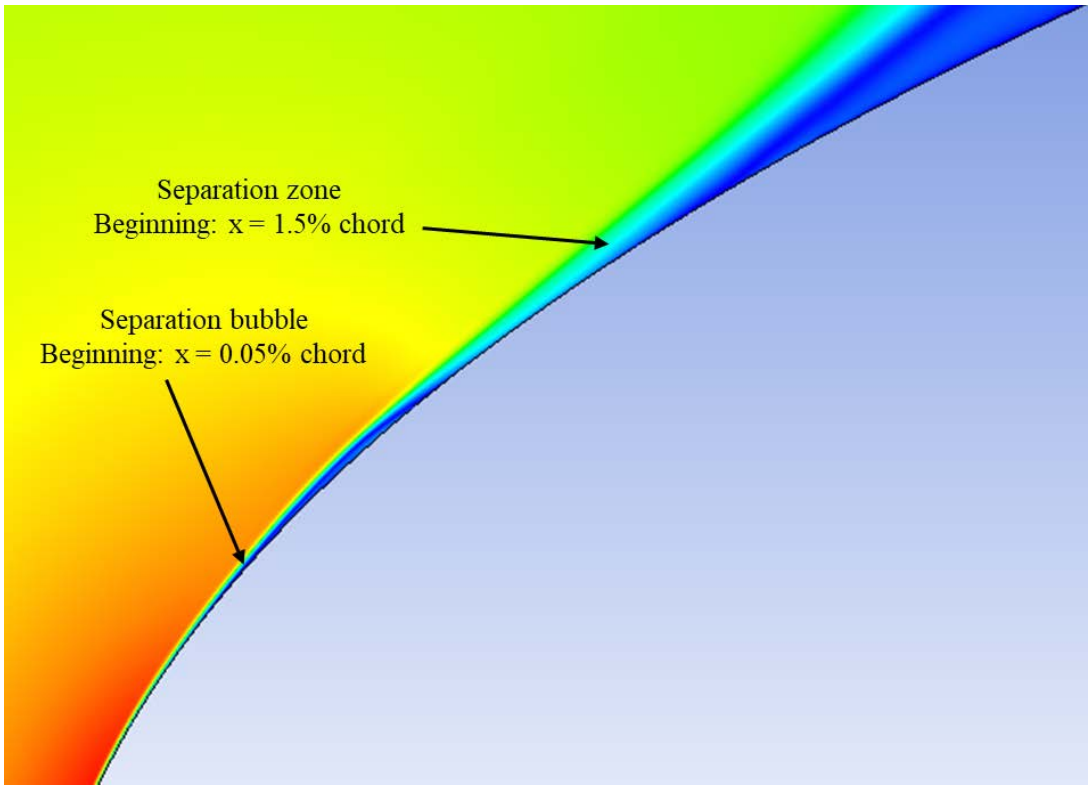

Figure 27. AoA 18˚ Re 3 Million, separation bubble and zone

4. Cause of Drag Discrepancy

Accurately predicting the separation bubble is very difficult. While the separation bubble is a very small feature, it affected the drag coefficient. The discrepancy between experimental and CFD results at and above an eight degree AoA is in part due to the presence of the separation bubble.

Predicted flow separation earlier than the experimental results likely caused an over prediction in drag. In order to investigate this possibility, the boundary layer at every 10 percent chord was plotted and non-dimensionalized for three cases. The first case was a two-degree AoA with good agreement with experimental results. Figure 28 displays the velocity flow field around the NACA 0012 airfoil at a two-degree AoA. A stagnation point near the leading edge of the airfoil is followed along the top of the airfoil with an increase in velocity. The flow remains attached over virtually the entire airfoil.

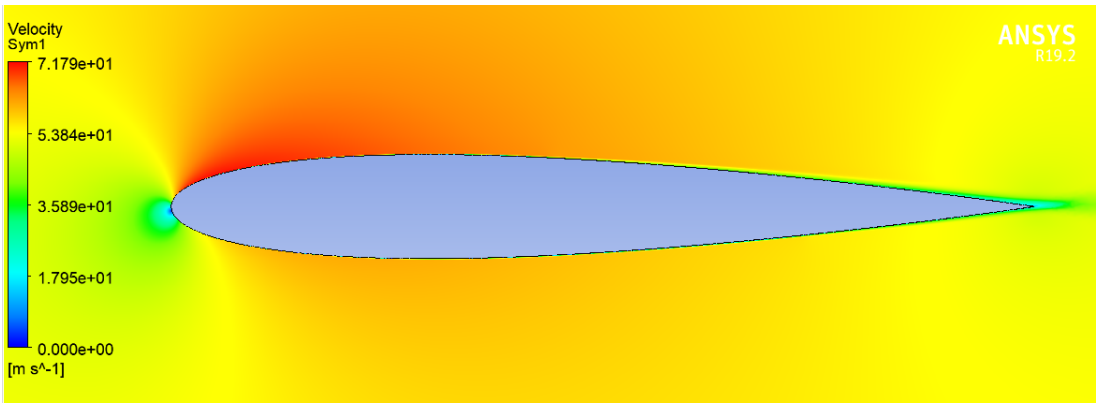

Figure 28. AoA 2,˚ Reynolds number 3 Mil, NACA 0012 velocity flow field

Figure 29 displays the velocity flow field around NACA 0012 airfoil at eight-degree AoA at Reynolds number of 3 million. Zero velocity is displayed as the blue region near the leading edge and at the trailing edge of the airfoil. The blue region at the trailing edge indicates that the local velocity in that region is slowing, but not necessarily separated.

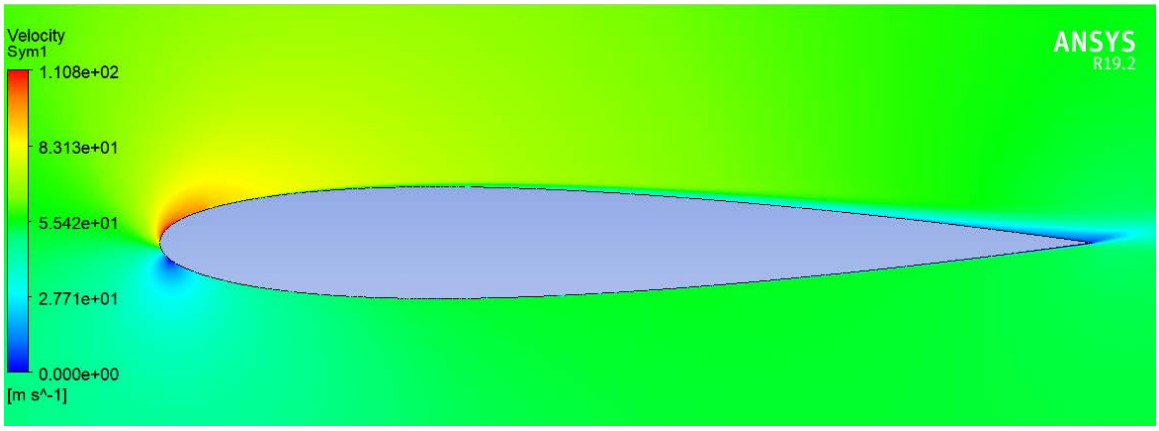

Figure 29. AoA 8˚, Reynolds number three million, NACA 0012 velocity flow field

Figure 30 displays the boundary layer profiles at ten percent increments along the chord length. At 10 percent chord there is a laminar boundary layer that is fully attached. A laminar boundary layer persists with ever-increasing velocity gradient until 40 percent chord. Between 40 and 50 percent chord transition occurs to a turbulent boundary layer.

The transition from laminar to turbulent boundary layer decreases the velocity gradient from the wall making the flow more attached. The velocity gradient increases, becoming less attached through the trailing edge of the airfoil. The flow remains attached across the entire upper surface of the airfoil.

Figure 31 displays the boundary layer profile at an AoA of eight degrees at every 10 percent chord for a NACA 0012 at a Reynolds number of three million. Boundary layer transition from laminar to turbulent flow occurs between 0 and 10 percent chord. The velocity gradient increases from the leading edge to trailing edge of upper airfoil surface. At 98 percent of the chord the velocity gradient has increased significantly, but is still attached. CFD, therefore, predicted an attached flow from the leading edge to the trailing edge of the airfoil.

Figure 32 displays the boundary layers across the NACA 0012 at Reynolds number of three million at an AoA of 12 degrees. At 90 and 98 percent of the chord the boundary layer velocity approaches zero indicating separation. In order to obtain more information about the separation of the flow at 90 and 98 percent chord these boundary layers were plotted separately in Figure 33.

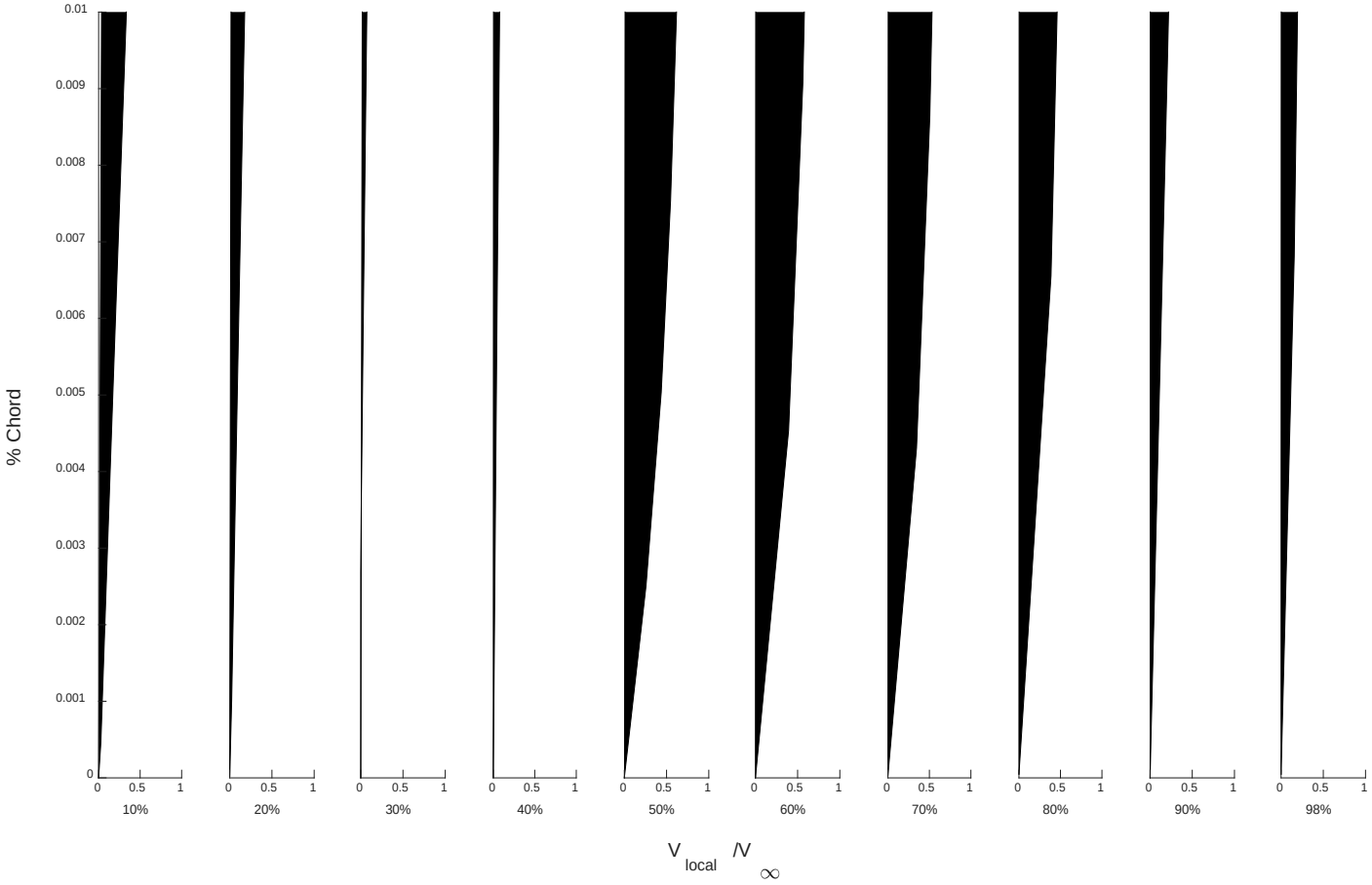

Figure 30. AoA 2˚ Reynolds number three million, boundary layer plots across chord

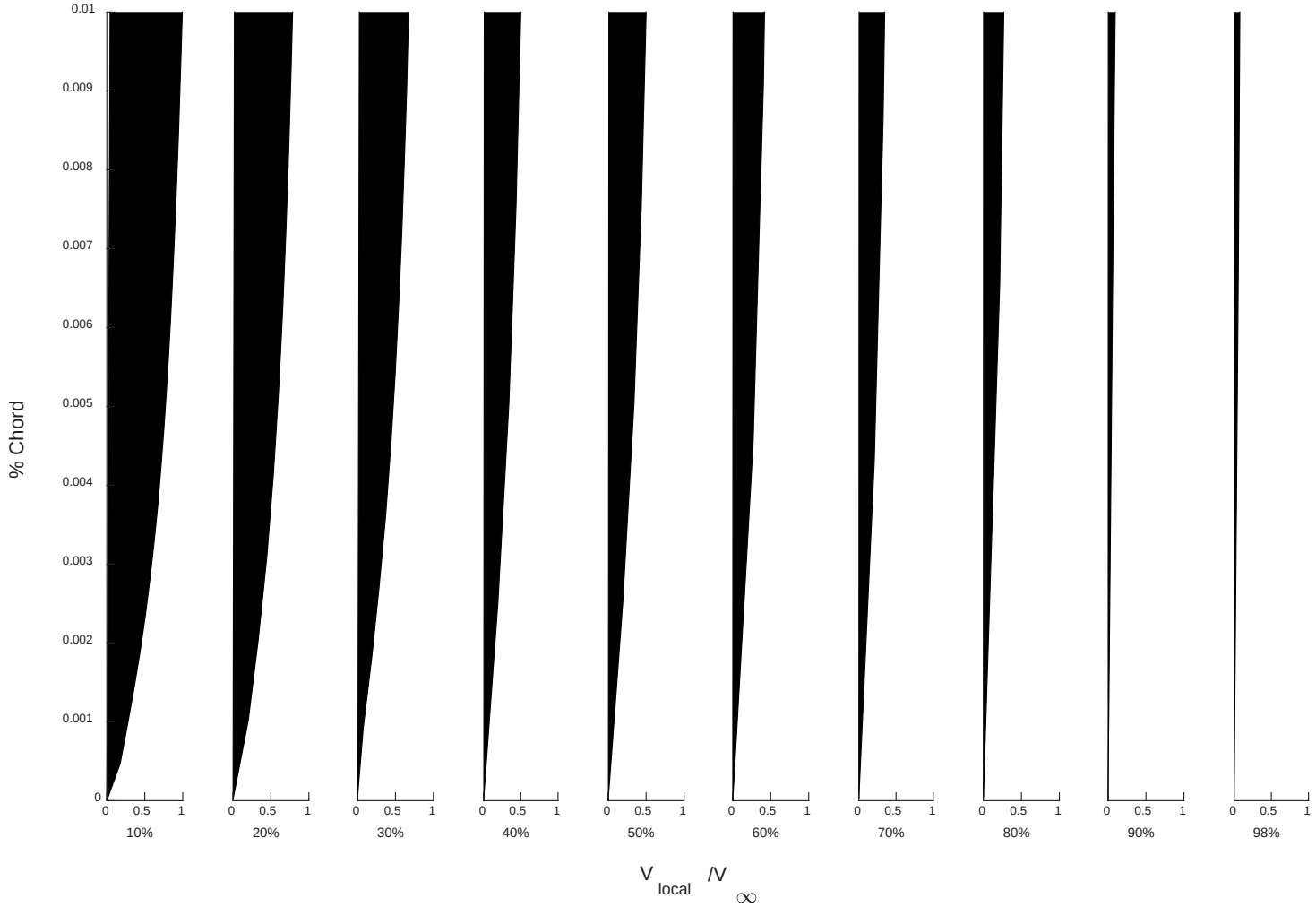

Figure 31. AoA 8˚ Reynolds number three million , boundary layer plots across chord

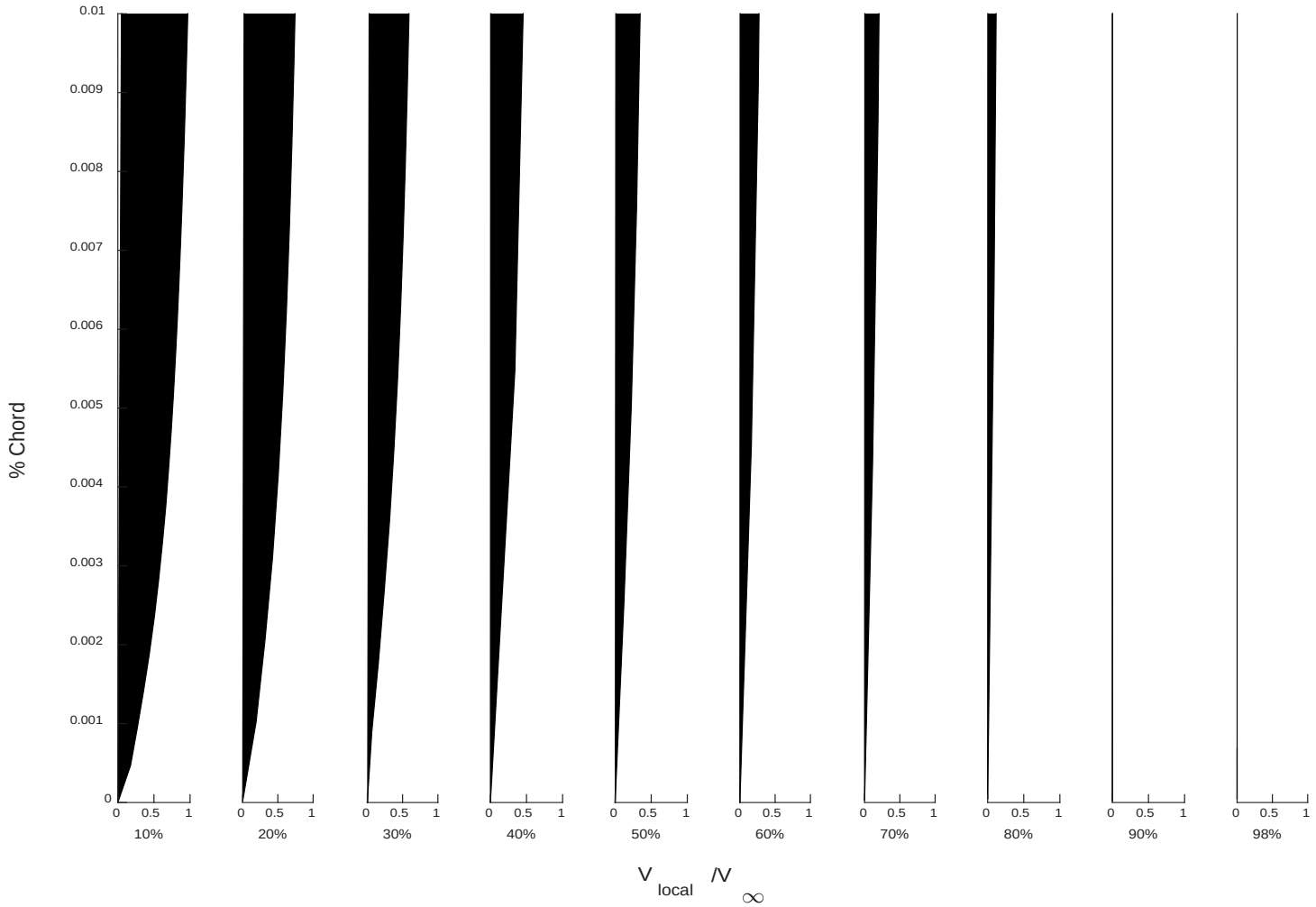

Figure 32. AoA 12˚ Reynolds number three million , boundary layer plots across chord

Figure 33 displays the 90 and 98 percent chord boundary layers. The 90 percent chord displays zero velocity until 0.02 percent chord, indicating the start of conditions for separation. The boundary layer at 98 percent chord shows flow reversal at the surface indicating the presence of separated flow.

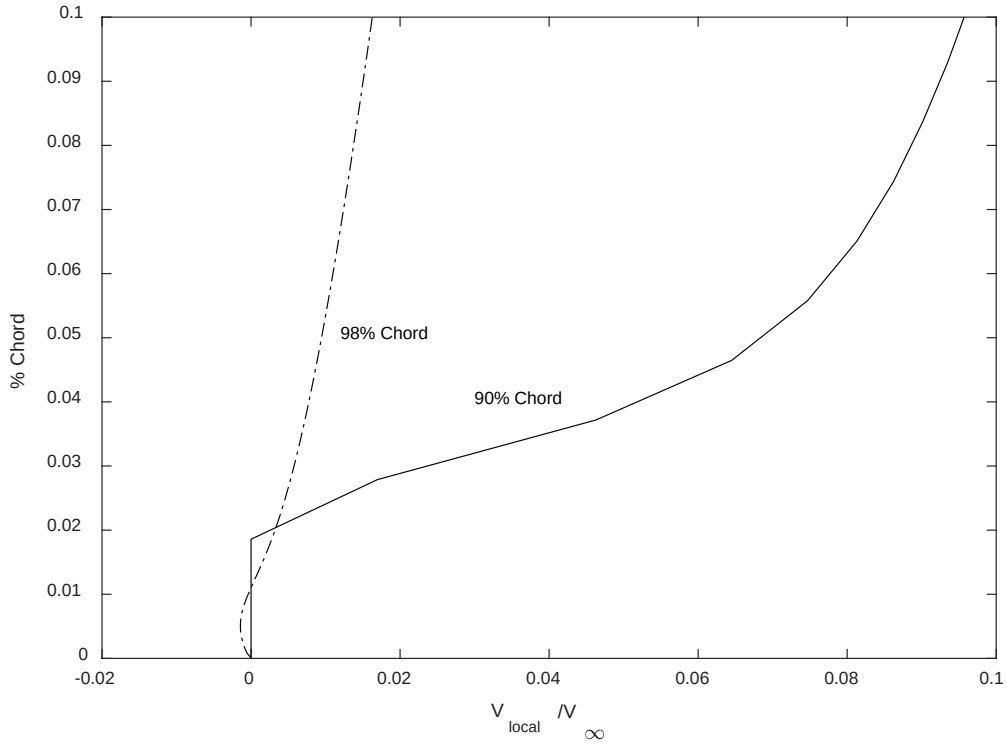

Figure 33. AoA 12˚, 90 and 98 percent chord boundary layers

The flow at two and eight degrees AoA was attached from leading edge to trailing edge. Separated flow was shown to occur at 12 degrees AoA, as shown in Figure 33. CFX's prediction of separated flow at a 12 degree AoA is likely the source for the discrepancy in drag coefficient from the experimental results.

The skin friction coefficients for two- and eight-degree AoA's were plotted in Figure 34. At the transition from laminar to turbulent boundary layer a jump is seen in the skin friction coefficient. The top (suction side) of the airfoil the transition occurs between the 0 and 0.1 of the chord at an AoA of eight degrees. Transition occurs between 0.4 and

0.5 location along the chord at an AoA of two degrees. This observation matches what is seen in Figure 30 and Figure 31.

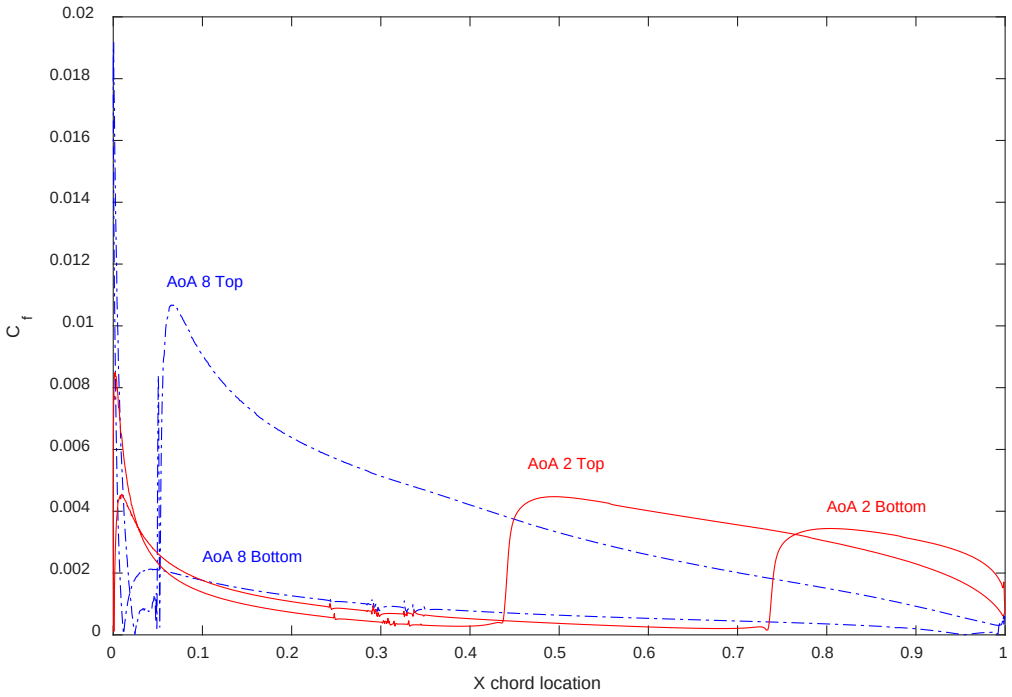

Figure 34. Skin friction coefficient at AoA 2˚ and 8˚ at Re 3 million

5. Nowak Result Comparison Skin Friction Coefficient Comparison

To further validate and investigate the drag results of the single element model the skin friction coefficient was plotted against the X chord location. These results were compared to the drag results found by Nowak [15].

Figure 35 displays the skin friction coefficient plotted against the chord at 0 degree AoA and a Reynolds number of six million. The transition from laminar to turbulent boundary layer occurred between 0.4 and 0.5 along the chord. The CFX results predicted a rapid transition. While Nowak's results predicted a far more gradual transition.

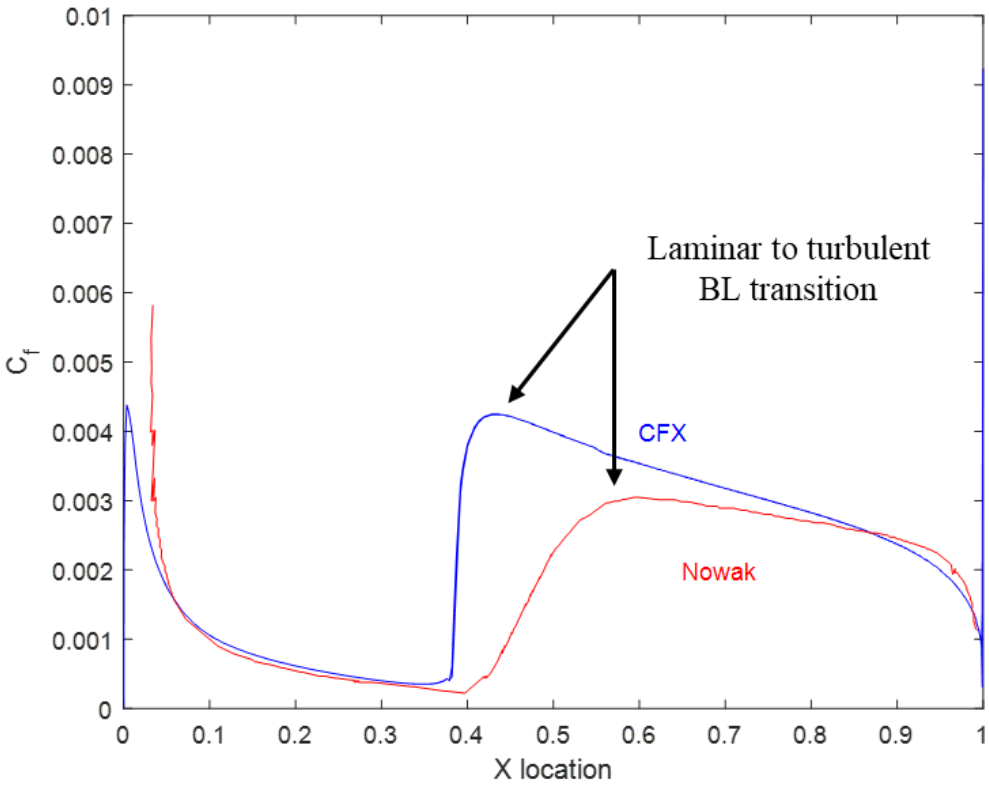

Figure 35. NACA0012 AoA 0˚, Reynolds number six million: skin friction coefficient comparison

To further investigate the skin friction coefficient across Reynolds numbers. CFX and Nowak's skin friction coefficient versus chord location were plotted in Figure 36. In this particular case CFX predicted transition from laminar to turbulent boundary layer far later than Nowak's results.

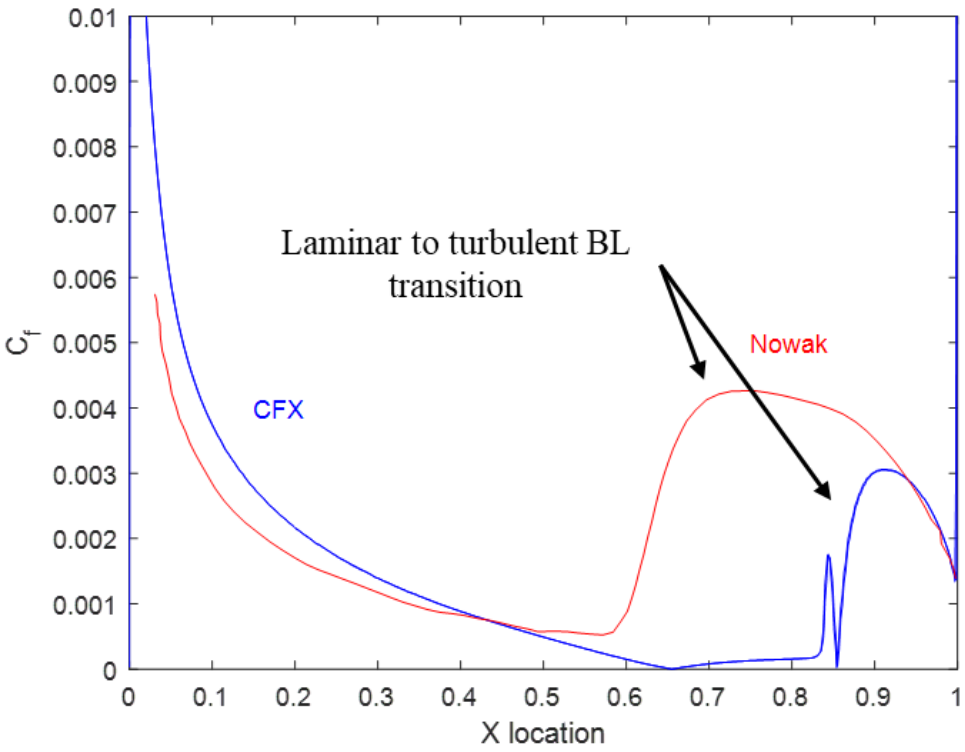

Figure 36. NACA0012 AoA 0˚, Reynolds number 540,000: skin friction coefficient comparison

B. TWO ELEMENT AIRFOIL CASE STUDY

Two test cases were conducted to validate the flow results with existing research and to compare results with the single element and cloth sail airfoils.

a. Convergence and Yplus Values

The Yplus variable for the Gentry and airfoil comparison test case ranged from 0.13 to 0.5 for all AoAs. Figure 37 displays the convergence history for the two-element airfoil at an AoA of four degrees at a Reynolds number of one million for comparison with the single element and cloth sail airfoils. The mass and momentum RMS values converged between 1e-4 and 1e-6. Similar convergence values and patterns were observed for the simulations other AoAs.

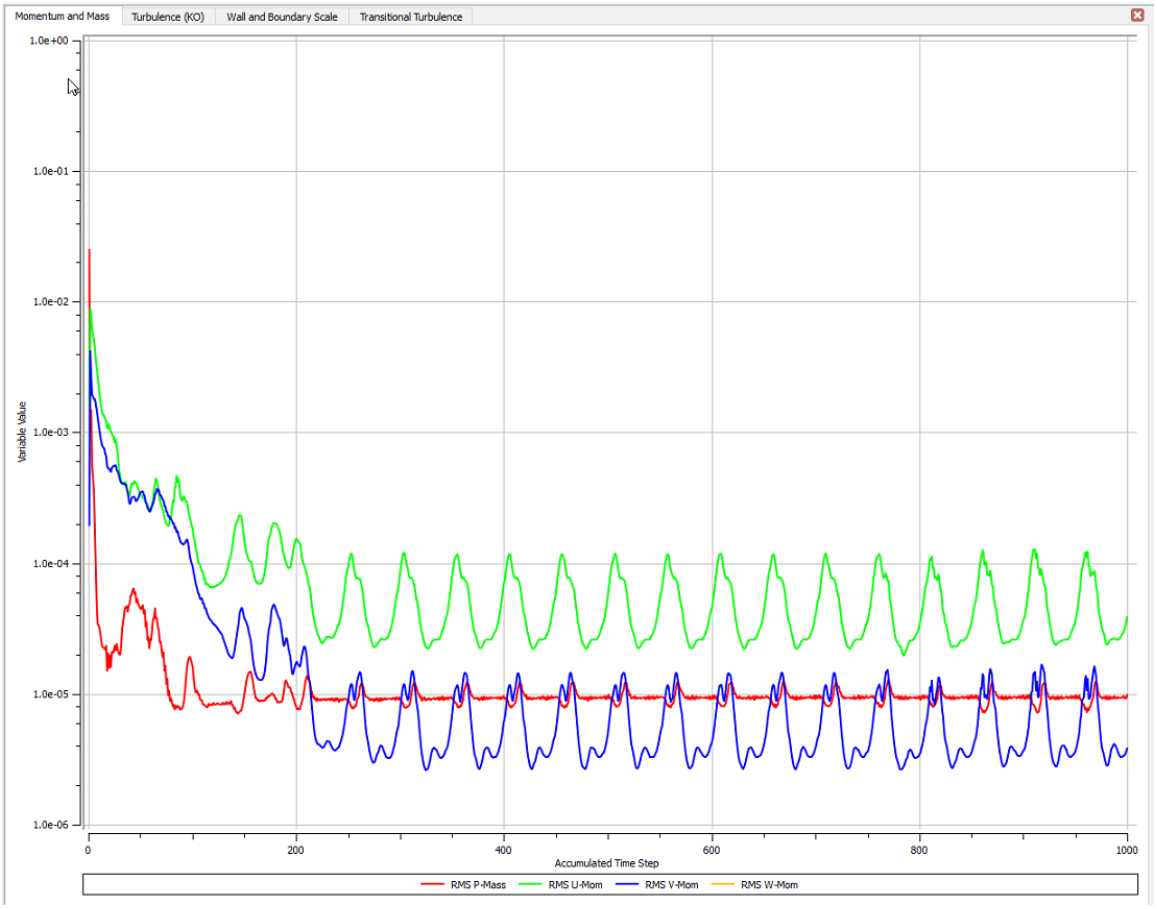

Figure 37. AoA 4˚ Reynold number 1 million 2 element comparison test case

b. Results Flow Analysis

Figure 38 displays the flow field across the Gentry geometry at an AoA of 10 degrees. The pressure coefficient of this flow filed was compared to the pressure coefficient provided in the paper to validate the CFX model.

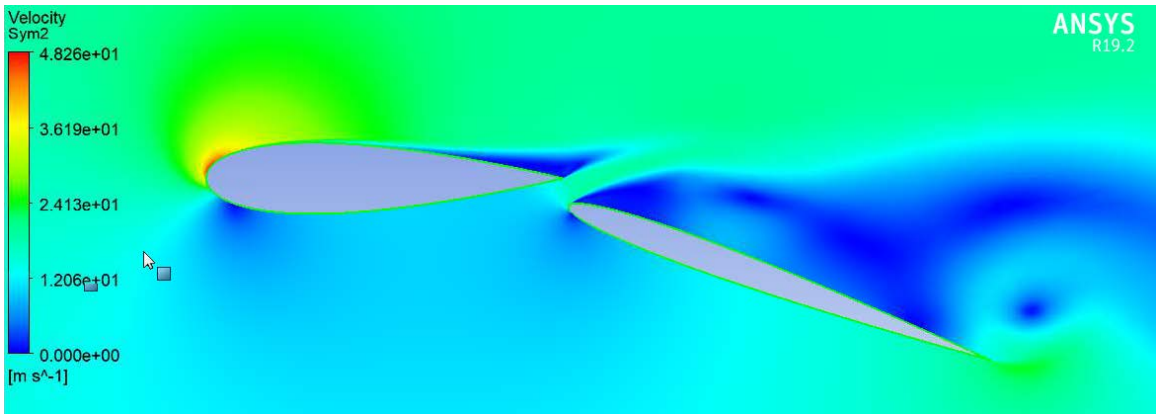

Figure 38. Gentry test case flow field at a 10˚ AOA

Figure 39 displays the pressure coefficient given in the Gentry test case as compared to results obtained from the CFX simulation. The front airfoil shown from zero to one displays a very similar pressure coefficient to the one found in the Gentry test case. The second airfoil from chord of one to 2.2 shows significant disagreement with the Gentry test case. The article did not give the AoA or displacement of the second airfoil. The large disagreement is likely due to a different airfoil deflection between the CFX model and the Gentry model.

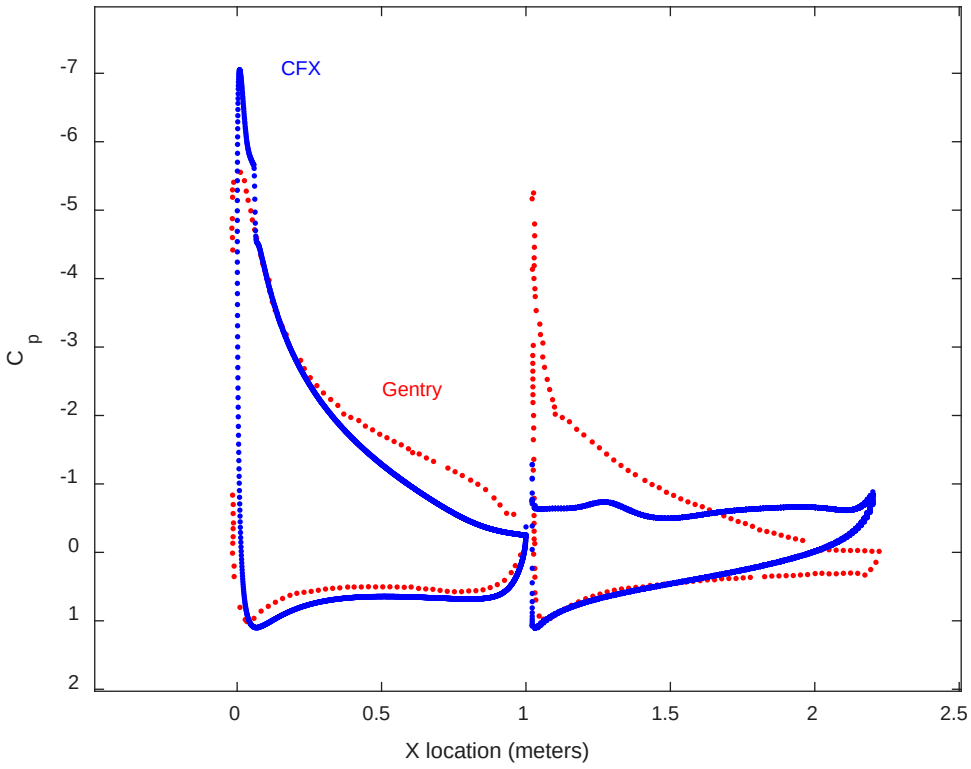

Figure 39. Gentry and CFX 10˚ AoA pressure coefficient comparison

The two-element airfoil used for comparison is displayed in Figure 40. Figure 40 displays the velocity flow field over the two-element airfoil at four-degree AoA. At a four-degree AoA the flow remains attached across both airfoils.

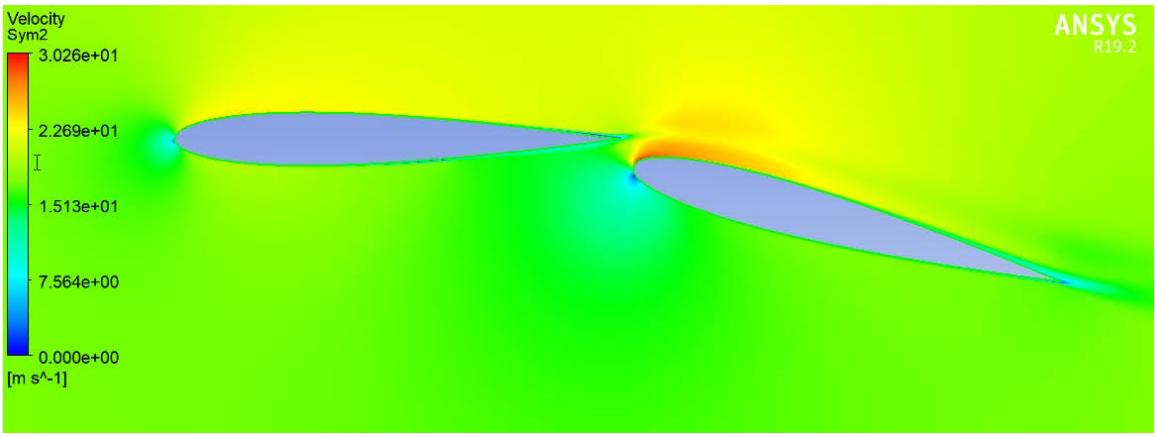

Figure 40. AoA 4˚ Reynolds number 1 million, two-element comparison

Figure 41 displays the two-element airfoil at a 12 degree AoA at a Reynolds number of one million. Both airfoils display separated flow, indicating a stall. The two-element airfoil stalled before the single-element airfoil. The single element airfoil stalled around an AoA of 16 degrees.

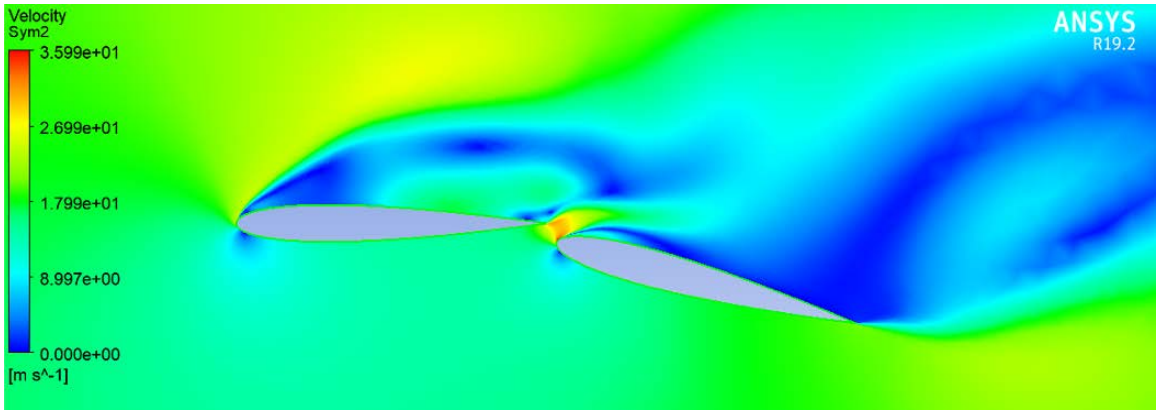

Figure 41. AoA 12˚ Reynolds number 1 million, two-element comparison

C. CLOTH SAIL AIRFOIL CASE STUDY

Two simulations were conducted to validate the CFX simulation and to compare the cloth airfoil to the single and two-element airfoils.

1. Convergence and Yplus

The boundary layer was not captured effectively by the cloth sail's mesh. The Yplus variable for the cloth sail ranged from 10 to 14. This is a very high range for Yplus seeking to accurately capture the boundary layer and drag of the airfoil.

Figure 42 and Figure 43 display the convergence history for the Avila comparison and the 14-degree AoA test case ran to compare results with the other airfoils. The Avila test case converged with all mass and momentum RMS values falling below 1e-6.

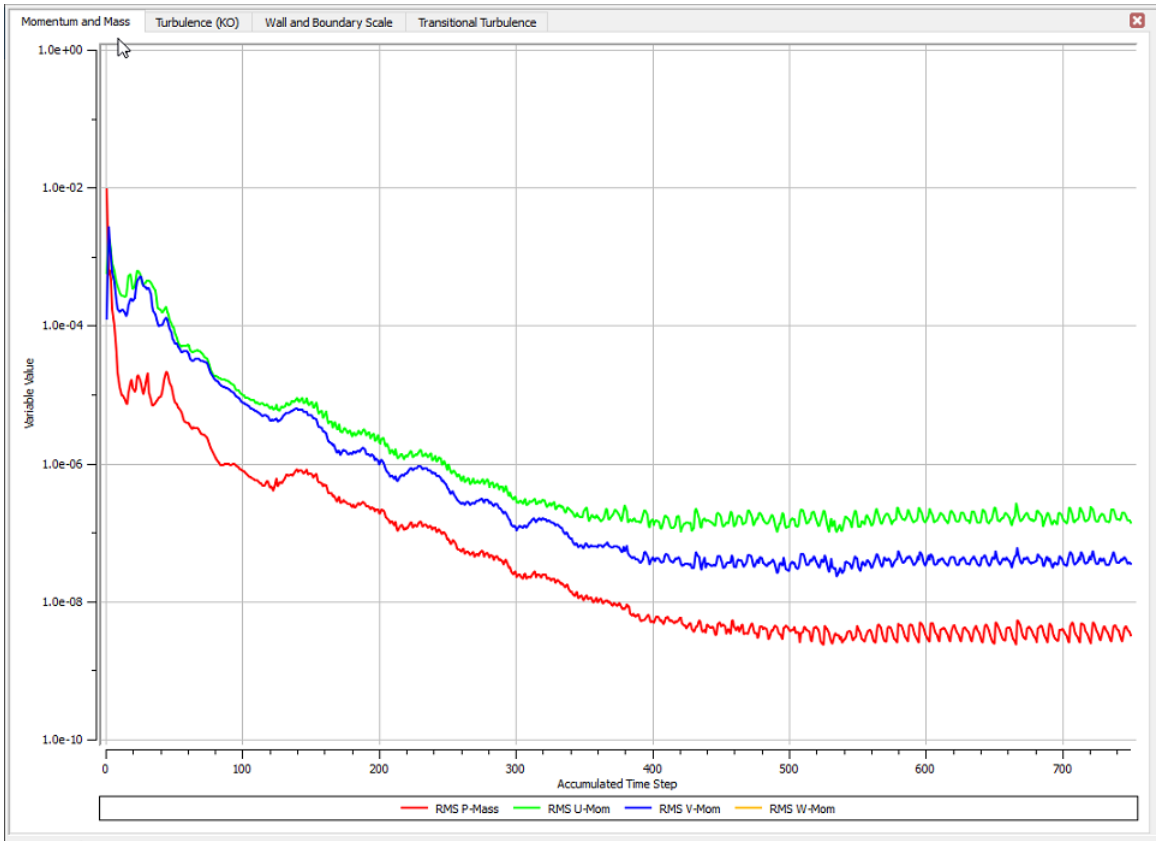

Figure 42. Avila test case convergence: AoA 10˚ Reynolds number 800,000

The comparison test case for an AoA of 14-degree displayed mass and moment RMS values converging between 1e-4 and 1e-6. The other AoA's displayed similar or better convergence than the 14-degree AoA test case.

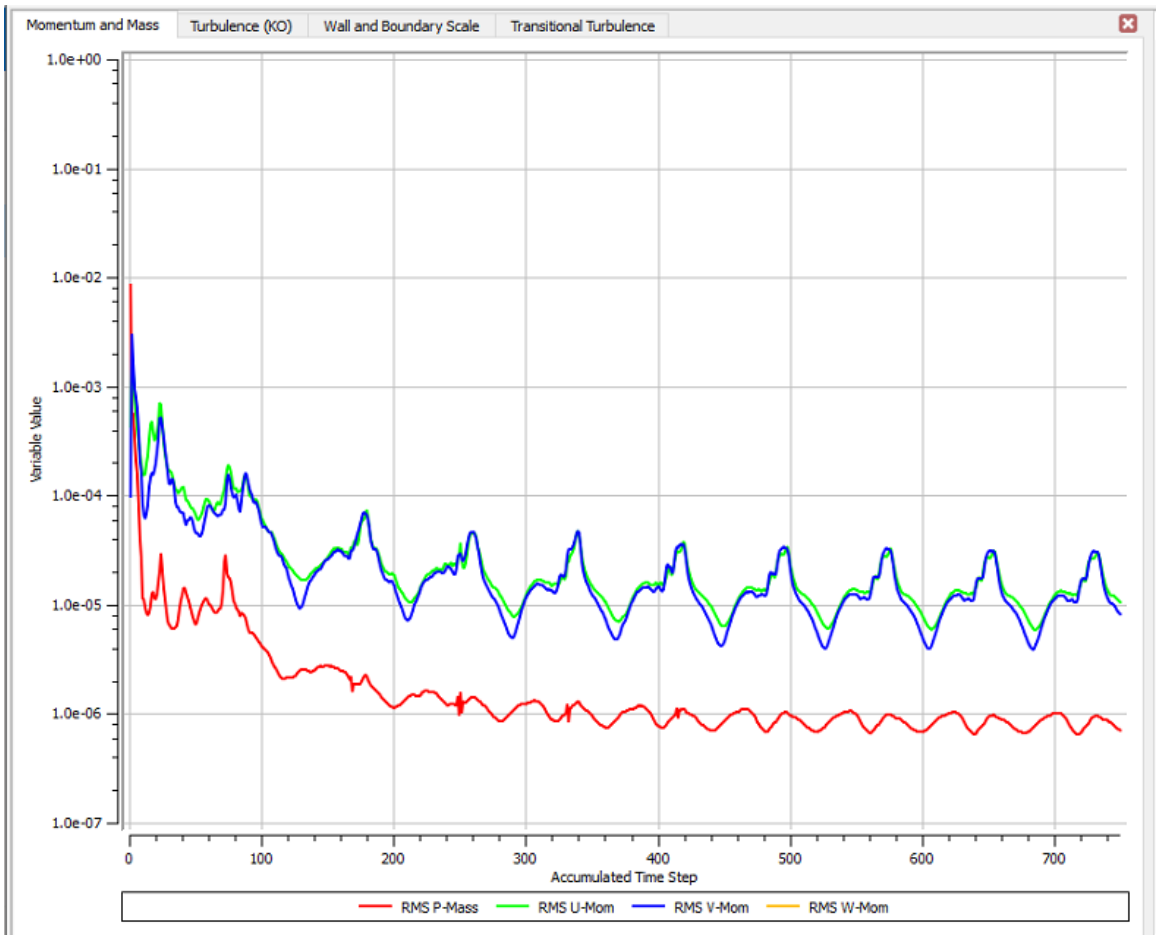

Figure 43. 14˚ AoA, Reynolds number one million, mass and momentum convergence versus time step

2. Avila Pressure Coefficient Comparison

Figure 44 displays the pressure coefficient versus chord location for both CFX and Avila (source [8]) results at a Reynolds number of 800,000. From regions 0.1 to 0.3 chord CFX results display oscillations in the pressure coefficient and a lower predicted pressure coefficient than the Avila results. This region is likely caused by a too coarse of a mesh. Near the mast there are additional discrepancies between the CFX and Avila results. This is likely due to slight differences in Avila's geometry and the geometry used in the CFX simulation to model the mast. The rest of the simulation matches Avila's results well.

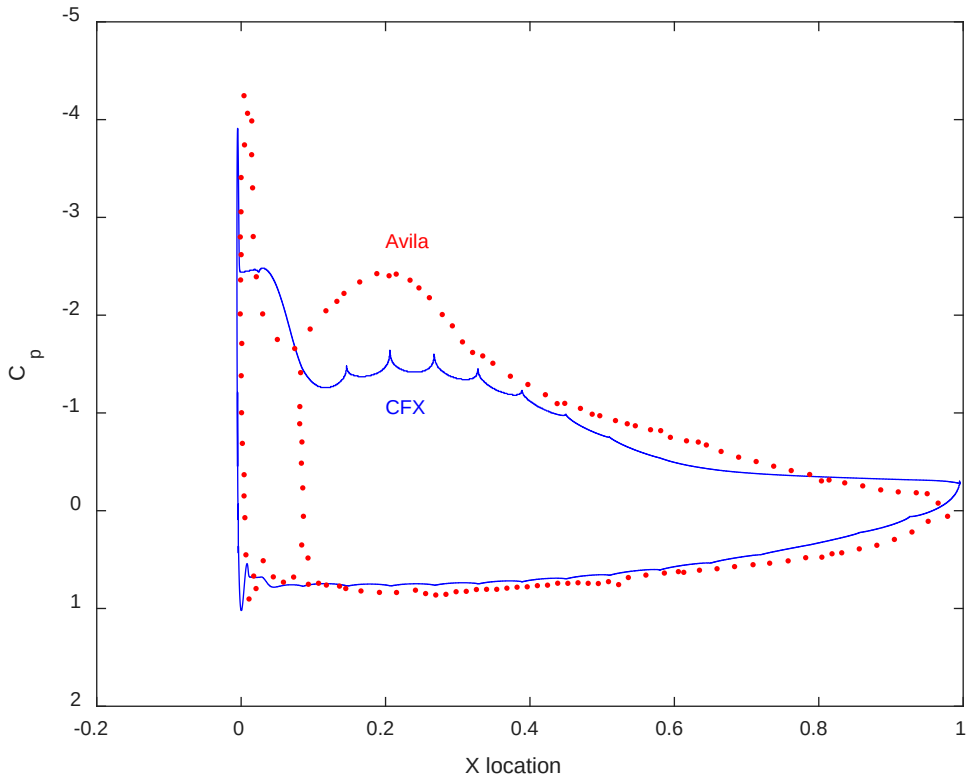

Figure 44. 10˚ AoA CFX and Avila Navier-Stokes solution comparison

Figure 45 displays the velocity distribution across the cloth airfoil at an AoA of 10 degrees and Reynolds number of 800,000. The region directly following the mast creates detached flow. Following the mast, the fluid reattaches to the sail. Due to a lack of an inflation layer to properly capture the boundary layer. The pressure coefficient oscillations from 0.1 to 0.3 on the suction side of the sail do not match the results provided by Avila.

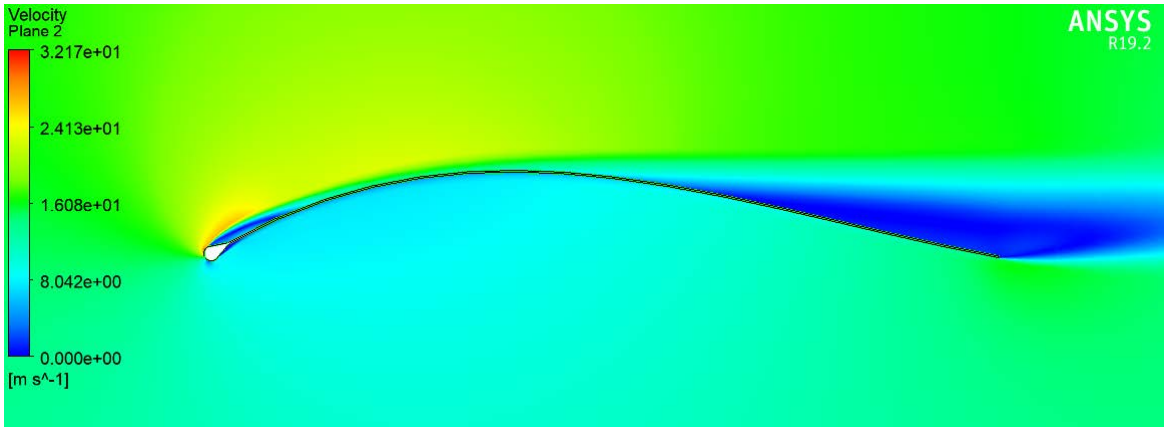

Figure 45. Velocity distribution AoA 10˚, Reynolds number 800,000

Figure 46 displays the pressure distribution over the cloth airfoil at a 10 degree AoA and Reynolds number of 800,000. Near the leading edge around the mast was the lowest pressure region.

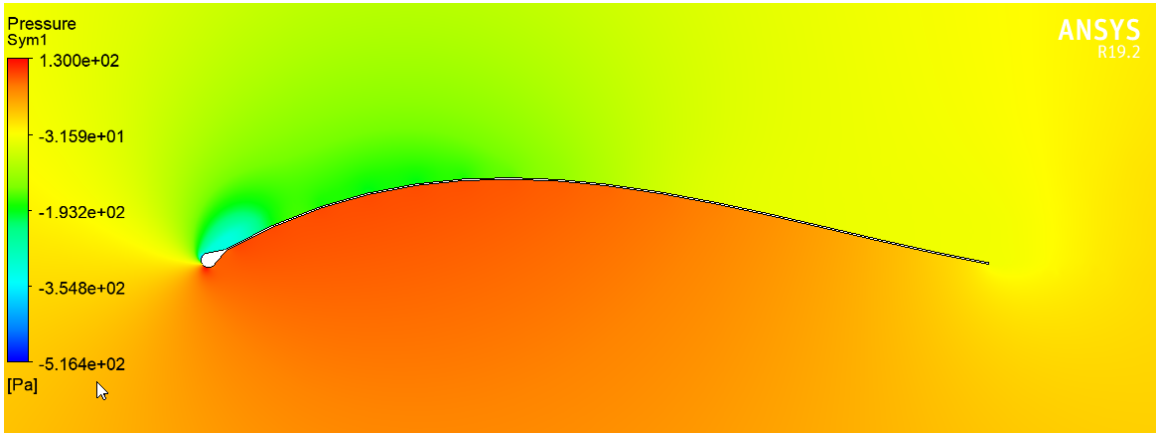

Figure 46. Pressure distribution AoA 10˚ Reynolds number 800,000

D. SINGLE, TWO-ELEMENT AND CLOTH SAIL AIRFOILS COMPARISON

After the validation and analysis of each model for the single, two-element, and cloth sail airfoils individually, the lift and drag coefficients for an AoA sweep from minus four degrees to 20 degrees were collected and plotted to compare the performance of each airfoil type.

Figure 17 displays the lift coefficient versus AoA for the single, two-element, and cloth sail airfoils. The single element airfoil displayed the lowest lift coefficient because it was symmetric. The two-element and cloth airfoils were cambered and showed a greater lift coefficient with AoA.

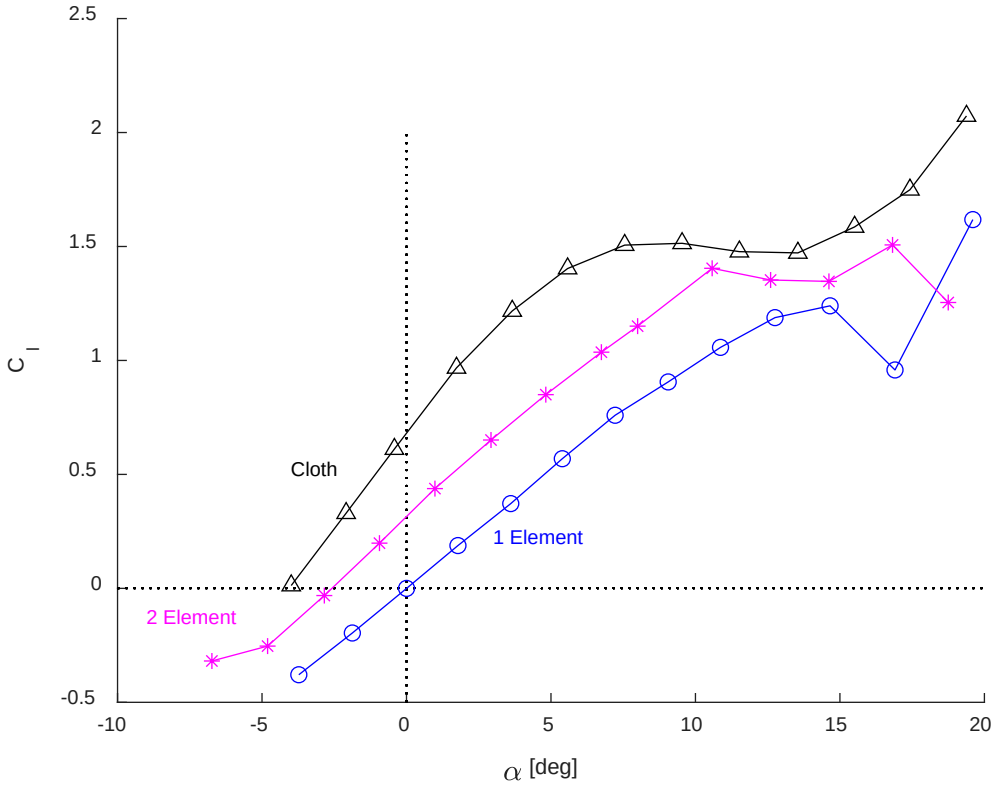

Figure 47. Lift coefficient versus AoA for all three airfoils

Figure 48 displays the drag coefficient versus lift coefficient for all three airfoils. The cloth airfoil displayed the greatest drag coefficient. The two-element airfoil displayed the lowest drag coefficient across the greatest range of lift coefficients. The single element airfoil displayed almost zero drag coefficient at or close to zero lift coefficient because of its symmetric shape.

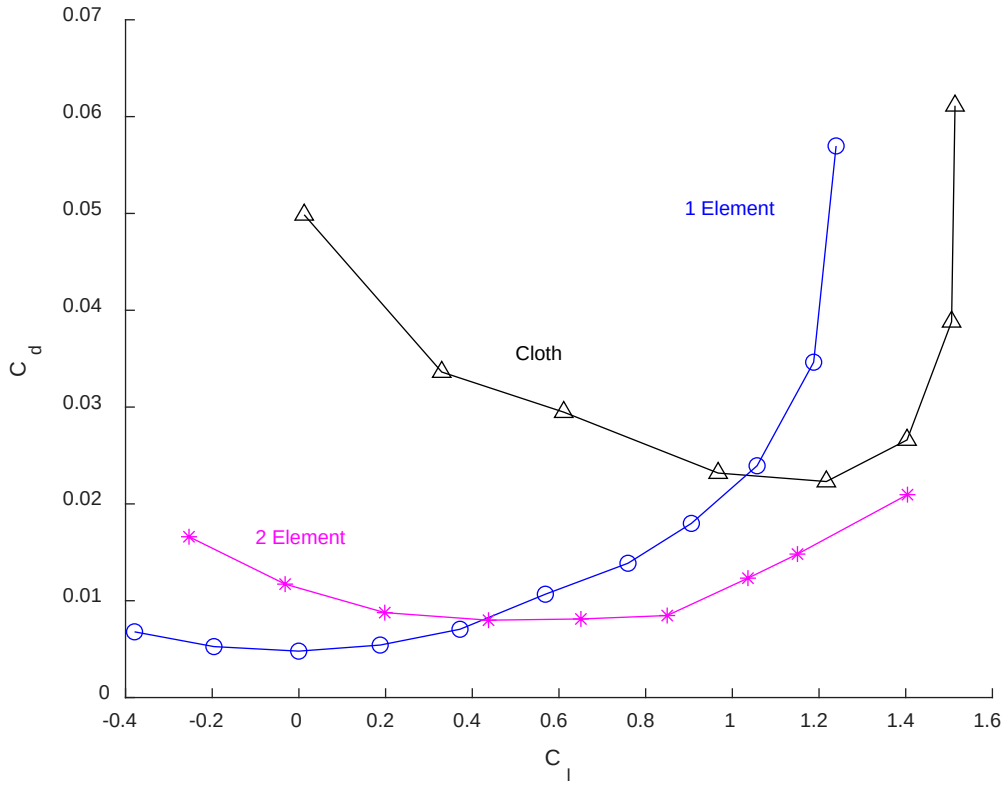

Figure 48. Drag polar for all three airfoils

Figure 49 displays the lift to drag ratio versus AoA for all three airfoils. This plot is the most telling and important for determining the best airfoil to produce the most thrust on a sailboat. The two-element airfoil outperformed the single and cloth airfoils significantly. The two-element airfoil at a 15-degree deflection yielded a lift to drag ratio almost twice as much as the single element cloth airfoils.

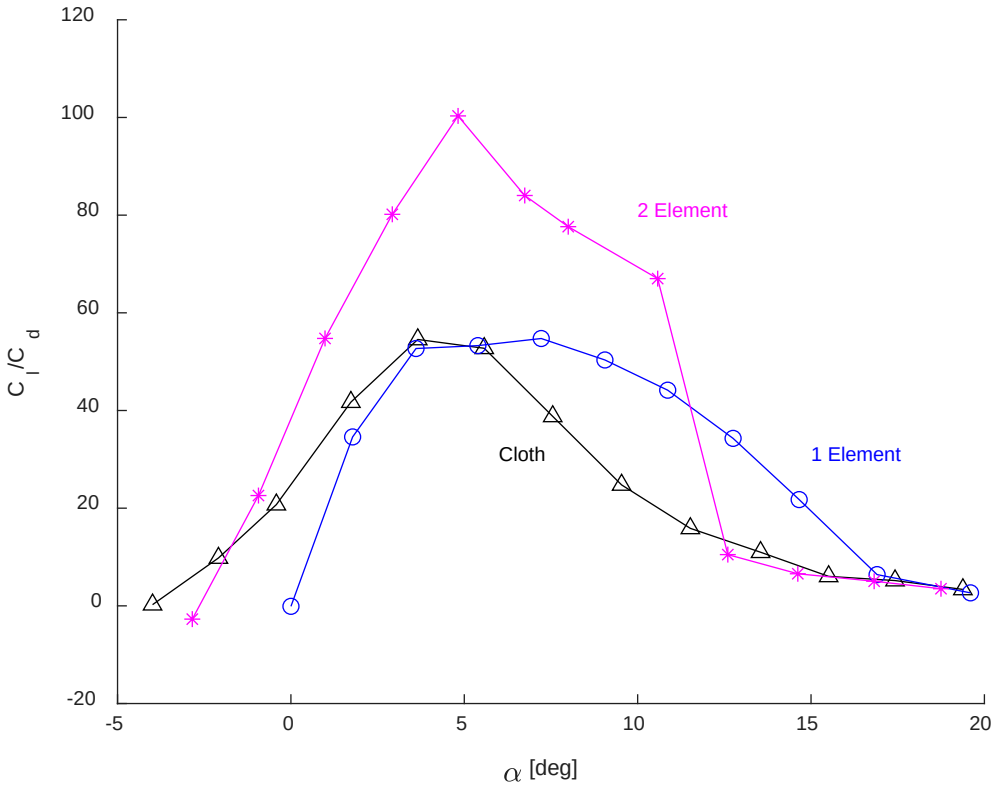

Figure 49. Lift to drag ratio of all three airfoils

V. CONCLUSION

A. AIRFOIL RECOMMENDATION FOR HYDROELECTRIC SAILBOAT

The best airfoil for the hydroelectric sailboat is the two-element airfoil, based on the superior lift to drag ratio of this airfoil. The single and cloth airfoils performed almost half as efficiently as the two-element airfoil. Furthermore, a two-element airfoil design allows for deflection adjustments to achieve the most efficient sail set-up for a given environment that the single element airfoil does not offer.

It should be noted that modeling a cloth sail accurately is very difficult with many variables that were not all captured in this simulation. A cloth airfoil exhibits laminar and turbulent boundary layers. Transition from laminar to turbulent boundary layer is difficult to predict and strongly dependent on the shape of the sail which is subject to small adjustments and changes based on the sailing conditions.

B. AREAS FOR ADDITIONAL RESEARCH

Additional CFD and experimental research should be conducted in the performance of cloth sails at various AoA's and shapes along a sailboat. It should be noted, a two-element rigid sail has shown to be unstable in applications such as the America's Cup [2]. A method to shrink and expand sail is necessary to effectively implement this design to weather thunderstorms and high winds.

An additional design consideration is simplicity and cost of construction. The two-element sail's lift over drag curve performed the best, however, the design and manufacture of a wingsail would be more difficult and time consuming than that of a cloth sail. A cloth sail would be cheaper and simpler to manufacture. Additionally, cloth sails are easily adjustable and lowered if necessary during strong winds and storms.

THIS PAGE INTENTIONALLY LEFT BLANK

APPENDIX A. GEOMETRY AND MESH CREATION GUIDE

To create a viable mesh with the necessary inflation layers to capture the boundary layer the geometry used to generate the airfoils is crucial. The following instructions outline how this geometry was achieved, and the meshing settings used to achieve a Yplus of under one for both the single and two-element airfoils.

A. SOLIDWORKS AIRFOIL GEOMETRY GENERATION

The first step is to import a series of coordinates to outline the airfoil curve. In order to achieve a smooth curve many points are needed. 1001 points were found suitable to create a smooth curve. The code used to generate these coordinates is including in Appendix C. NACA Airfoil Coordinate Generation Code. This code was provided courtesy of Dr. Garth Hobson via personal communication [18].

Once the x and y coordinates of the airfoil curve were generated the coordinates were saved as a text delimited (txt) file to import into Solidworks (a commercial solid modelling program). In Solidworks, the first step in creating the geometry was to sketch a box and extrude out two millimeters. The airfoil coordinates were then imported into Solidworks. When the airfoil coordinates are imported into Solidworks the program does not treat the coordinates as part of the drawing. Therefore in order to make the curve part of the sketch the “Convert Entities” button must be used. The new line drawn around the curve is now a spline.

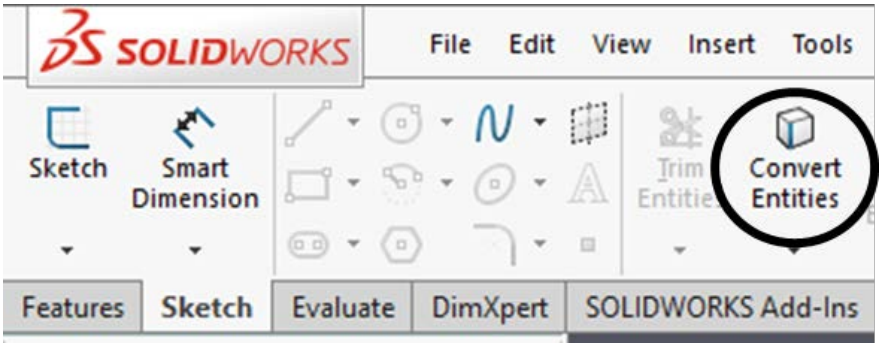

Figure 50. Convert entities button used to create a spline in Solidworks

This new spline can then be moved and rotated as is necessary for the desired geometry. Finally an extruded cut, using the setting “through all-both” was used to cut the airfoil out of the box previously extruded. This method creates a smooth airfoil with sharp trailing edge. A sharp trailing edge was key to generating a mesh with inflation layers.

B. MESH GENERATION

Three mesh parameters were used to create the mesh within ANSYS CFX: edge sizing, sweep method, and inflation. The global mesh sizing was set to an element size of 0.1 meters, 1.1 growth rate, and 0.1˚ curvature normal. All other global mesh settings were left at their default values in CFX. In order to create a mesh using both an inflation and sweep method source [19] was referenced. The sweep method must be set for the entire body and all tri free face mesh type. Figure 51 displays the sweep method settings used.

Scope	
Scoping Method	Geometry Selection
Geometry	1 Body
Definition	
Suppressed	No
Method	Sweep
Element Order	Use Global Setting
Src/Trg Selection	Manual Source and Target
Source	1 Face
Target	1 Face
Free Face Mesh Type	All Tri
Type	Number of Divisions
Sweep Num Divs	Default
Element Option	Solid
Advanced	
Sweep Bias Type	No Bias

Figure 51. Sweep method parameters

To create an inflation layer simultaneously with the sweep method the front face of the volume box must be selected as the scope geometry. The airfoil edge must be selected as the boundary scoping method. Figure 52 displays the inflation layer settings used in conjunction with the sweep method.

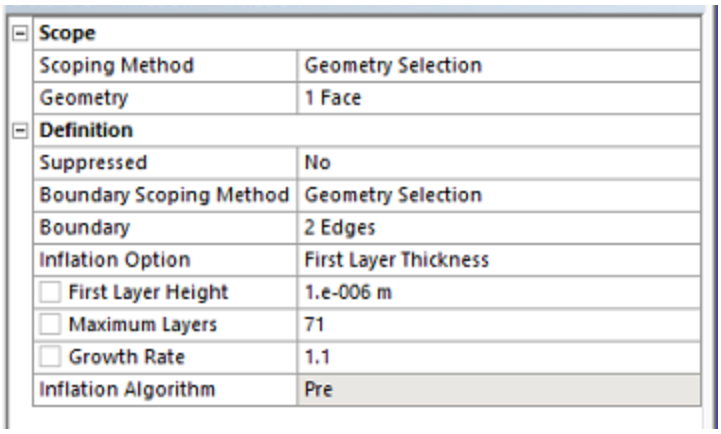

Scope	
Scoping Method	Geometry Selection
Geometry	1 Face
Definition	
Suppressed	No
Boundary Scoping Method	Geometry Selection
Boundary	2 Edges
Inflation Option	First Layer Thickness
First Layer Height	1.e-006 m
Maximum Layers	71
Growth Rate	1.1
Inflation Algorithm	Pre

Figure 52. Inflation layer settings

Finally, to create a more detailed mesh an edge sizing was added to the airfoil. Figure 53 displays the edge sizing parameters used.

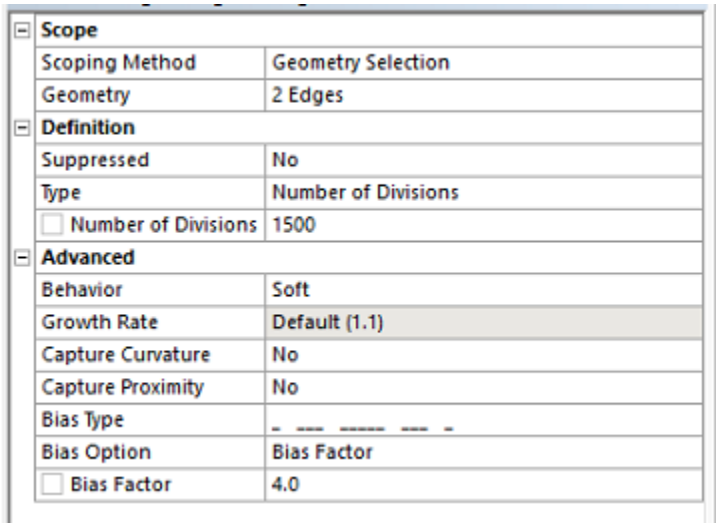

Scope	
Scoping Method	Geometry Selection
Geometry	2 Edges
Definition	
Suppressed	No
Type	Number of Divisions
Number of Divisions	1500
Advanced	
Behavior	Soft
Growth Rate	Default (1.1)
Capture Curvature	No
Capture Proximity	No
Bias Type	- --- ----- --- -
Bias Option	Bias Factor
Bias Factor	4.0

Figure 53. Edge sizing parameters

Figure 54 details the mesh created using the techniques and parameters discussed in this appendix.

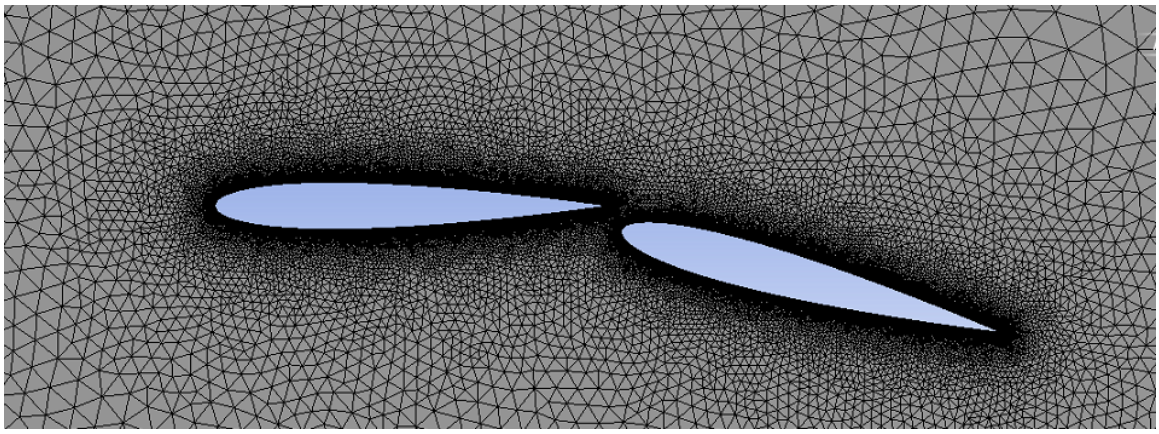

Figure 54. Final mesh two-element airfoil mesh

APPENDIX B. BOUNDARY LAYER PLOT TECHNIQUE CFD-POST

The following technique was used to create the boundary layer profiles seen plotted throughout this thesis. To obtain a boundary layer profile a line must be drawn perpendicular to the airfoil's surface. Solidworks was used to obtain the coordinates for these lines. Once the coordinates of the lines were determined a line was inserted in CFD-Post. Figure 55 and Figure 56 display the graphical user interface to input the line coordinates and the line created by that input.

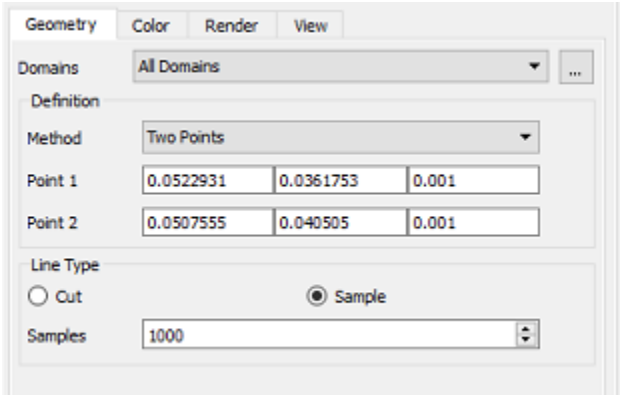

Figure 55. Line input coordinate interface

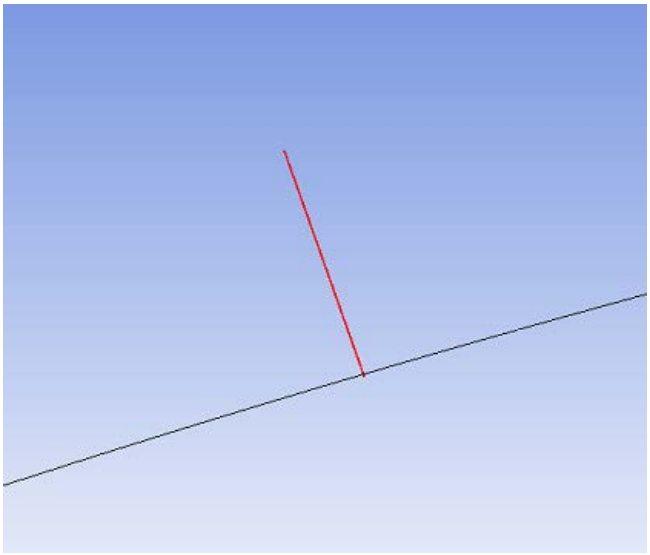

Figure 56. Inserted line to capture boundary layer

Following the insertion of a line, an expression must be entered to calibrate the starting position of the plot to zero. Equation (10) displays the distance equation used to calculate the vertical distance from the surface of the airfoil.

$$V = \sqrt{\left(x - x_o\right)^2 + \left(y - y_o\right)^2} \tag{10}$$

The variables x_o and y_o are the initial start points of the line at the surface of the airfoil. This equation must be converted into a variable to plot later. The final step toward creating a boundary layer is inserting the chart. The vector given in Equation (10) must be plotted versus the u-velocity component of the fluid flow solution. This process may be repeated in any location along the airfoil's edge to obtain the boundary layer profile.

APPENDIX C. NACA AIRFOIL COORDINATE GENERATION CODE

```
%------------------
%
%   VAWT Blade profile NACA00XX
%
%------------------
clear all
close all
format long
%
% Blade setting Angle
%

alpha = input('Angle of attack in degrees ')
if isempty(alpha)
   alpha = 0.0
end
alpha_deg=alpha
alpha=alpha*pi/180.0;
%
% NACA 00xx thickness
%


tau = input('Percent Thickness of a NACA 4-digit Airfoil, eg. NACA0012 type 12')
if isempty(tau)
   tau = 12
end
%
% Chord
%
c = input('Chord Length')
if isempty(c)
   c = 1
end

% No. of points around the airfoil
m = input('No. of points around the airfoil')
if isempty(m)
   m = 100
end

md2=m/2;
delt=pi/md2;
%
%   Cluster the points around the leading and trailing edges
%
```

```
for i=1:md2+1
    theta(i)=delt*(i-1);
    x(i)=0.5*(1.0+cos(theta(i)));
    y(i)=-5*(tau/100)*c*(0.2969*sqrt(x(i))-...
    0.126*(x(i))-0.3537*(x(i))^2+...
    0.2843*(x(i))^3-0.1015*(x(i))^4);
    x(i)=x(i)*c;
end

for i=md2+2:m+1
    theta(i)=delt*(i-(md2+1));
    x(i)=0.5*(1.0-cos(theta(i)));
    y(i)=5*(tau/100)*c*(0.2969*sqrt(x(i))-...
    0.126*(x(i))-0.3537*(x(i))^2+...
    0.2843*(x(i))^3-0.1015*(x(i))^4);
    x(i)=x(i)*c;
end

plot(x,y,'r.')
title(['NACA00',num2str(tau),' profile'])
axis([0 c -0.4*c 0.4*c])
grid on

%
%   Rotate the airfoil
%

for i=1:m+1
    X(i) = x(i)*cos(alpha)+y(i)*sin(alpha);
    Y(i) = x(i)*sin(alpha)-y(i)*cos(alpha);
end

hold on
plot(X,Y,'b')

%
%   Translate
%

DELX = 0.25*c
DELY = 0.8

for i=1:m+1
    XX(i) = X(i)-DELX;
    YY(i) = Y(i)+DELY;
end

figure(2)
plot(XX,YY,'b')
title(['NACA00',num2str(tau),' profile - Rotated & Translated'])
axis([-0.2*DELY DELY 0 1.2*DELY])
grid on
```

```
xyz=[XX;YY]';
xyz(:,3)=0;
xyz
```

Published with MATLAB® R2019b

THIS PAGE INTENTIONALLY LEFT BLANK

LIST OF REFERENCES

[1] N. S.-K. Max F. Platzer, "Mobile offshore platforms for power generation: The energy ship," *ASME*, pp. 1–7, 2018.

[2] Adam Fisher, "Winging It: America's Cup racers push the sailboat to its limits." *Wired*. https://www.wired.com/2011/08/ff_americascup/.

[3] J. Paton and H. Morvan, "Using computational fluid dynamics to model sail interaction-the 'slot effect' revisited," *J. Wind Eng. Ind. Aerodyn.*, vol. 97, no. 11–12, pp. 540–547, Dec. 2009, doi: 10.1016/j.jweia.2009.08.005.

[4] Z. Quezada, "Where are we going: Understanding points of sail . Learn to sail, sailing tips points of sail, sailing terms," accessed Mar. 23, 2020. [Online]. Available: https://asa.com/news/2019/02/14/points-of-sail/.

[5] I. M. Viola, "Downwind sail aerodynamics: A CFD investigation with high grid resolution," *Ocean Eng.*, vol. 36, no. 12–13, pp. 974–984, 2009. [Online]. doi: 10.1016/j.oceaneng.2009.05.011.

[6] P. Collie, S.J., Gerritsen, M.,Jackson, "A review of turbulence modeling for use in sail flow analysis," Auckland, New Zealand, 2001.

[7] Y. Zheng, D. Liu, H. An, W. Sun, and T. Xu, "Study on a comprehensive energy-saving sail by CFD method," *Open J. Fluid Dyn.*, vol. 06, no. 03, pp. 145–155, Sept. 2016. [Online]. doi: 10.4236/ojfd.2016.63012.

[8] M. R. Avila, "Computational and experimental investigation of the aerodynamic characteristics of a windsurfing sail section," M.S. thesis, Dept of Aero Eng., NPS, Monterey, CA, USA, 1992. [Online]. Available: https://calhoun.nps.edu/handle/10945/23577

[9] S. Wilkinson, "Static pressure distributions over 2D mast/sail geometries," *Mar. Technol.*, vol. 26, no. 4, pp. 333–337, Oct. 1989. [Online].

[10] A. F. H Amini, M Rad, and A. Fakhraee, "Comparison final velocity between sailing boat with a rigid airfoil and cloth sail," in *Proc. of IMEC2006*. [Online]. Available: https://asmedigitalcollection.asme.org/IMECE/proceedings-abstract/IMECE2006/47705/691/310178

[11] J. Yoo and H. T. Kim, "Computational and experimental study on performance of sails of a yacht," *Ocean Eng.*, vol. 33, no. 10, pp. 1322–1342, Feb. 2005. [Online]. doi: 10.1016/j.oceaneng.2005.08.008.

[12] P. I. Alza, “Numerical and experimental studies of sail aerodynamics,” Ph.D. Thesis, Univ of Madrid, Madrid, Spain, 2012. [Online]. Available: https://core.ac.uk/download/pdf/12001812.pdf

[13] Y. Cao, L. Chao, J. Men, and H. Zhao, “The efficiently propulsive performance flapping foils with a modified shape,” *Ocean. 2016 - Shanghai*, pp. 1–4, 2016. [Online]. doi: 10.1109/OCEANSAP.2016.7485337.

[14] I.H. Abbott and A.E. Von Doenhoff, *Theory of Wing Sections: Including a Summary of Airfoil Data.* New York, NY, USA: Dover Publications, Inc., 1949.

[15] L. M. Nowak, “Computational investigations of NACA 0012 airfoil in low reynolds number flows,” M.S. thesis, Aero Eng., NPS, Monterey, CA, USA, 1992.

[16] A. Gentry, “The application of computational fluid dynamics to sails,” in *Proc. of the Symp. of Hydro Perf. Enhanc for Marine App*, Seattle, Washington, 1988. [Online]. doi: 10.2514/6.1986-2651.

[17] *Ansys CFX-Solver Theory Guide*, ANSYS, Canonsburg, PA, USA, 2011. [Online]. Available: https://itrss.mst.edu/media/informationtechnology/itrss/documents/ansysdocs/ANSYS%20CFX%20Reference%20Guide.pdf

[18] G. Hobson, private communication, Jan. 2020.

[19] “Tips & tricks: Inflation layer meshing in ANSYS,” Leap Australia, 2012. [Online]. Available: https://www.computationalfluiddynamics.com.au/tips-tricks-inflation-layer-meshing-in-ansys/.

INITIAL DISTRIBUTION LIST

1. Defense Technical Information Center
   Ft. Belvoir, Virginia

2. Dudley Knox Library
   Naval Postgraduate School
   Monterey, California